First-principle calculations of ferroelectric properties of HfO_2 and ZrO_2

Aayesha Tariq

Department of Physics
Faculty of Mathematics and Natural Sciences

UNIVERSITY OF OSLO

Spring 2022

First-principle calculations of ferroelectric properties of HfO_2 and ZrO_2

Aayesha Tariq

Master thesis in Materials, Nanophysics and Quantum Technology

Supervisiors: Prof. Clas Persson &
Prof. Ole Martin Løvvik

UNIVERSITETET
I OSLO

First-principle calculations of ferroelectric properties of HfO_2 and ZrO_2

http://www.duo.uio.no/

Printed: Reprosentralen, University of Oslo

Abstract

Density functional theory (DFT) based methods have been used to describe the electronic, optical, and ferroelectric properties of Hafnium Dioxide (HfO_2) along with their binary oxide and Zirconium Dioxide (ZrO_2) using PBE and mBJ for three different phases. Corrective Hubbard (U) terms have been added to exchange-correlation energy better to reproduce the excited-state properties of hafnia and zirconia polymorphs. In the electronic properties, the density of states is calculated and analyzed in detail, along with real and imaginary parts of the dielectric function. As well as born effective charges are also estimated. The monoclinic and tetragonal phase resulted in the non-ferroelectric, while the orthorhombic showed peculiar properties due to its intrinsic ferroelectric behavior.

Contents

List of Figures

List of Tables

Acknowledgement

I would like to take this opportunity to thank all the people that helped me write this thesis. First, I would like to thank my supervisors, Clas Persson, Konstantina Iordanidou, and Ole Martin Løvvik, for your help, guidance, and motivation. Then I would like to thank the rest of the members of my research group for helpful discussions and great memories. The extended network at the The Centre for Materials Science and Nanotechnology also deserve gratitude. t I would like to thank my family, friends, and partner Muhammad Hammad for their patience and support throughout this process.

Part I

Introduction

In recent decades, the microelectronics industry has been observed to struggle with the expanded usefulness and execution of integrated circuits. That is to create quicker, more modest, and less expensive electronic devices. The thickness of cells on a chip is expanded by decreasing the base element size and creating additional complicated circuits. A lower working voltage should be applied when the component size decreases to keep a steady electrical field; this will require the capacitance to increment for the devices to work effectively. Since the capacitance is inversely proportional to the thickness of the insulating layer between the capacitors, this thickness is reduced accordingly.

The most commonly used capacitor material in random access memories and field-effect transistors is silicon dioxide SiO_2. Over the past few years, the successful scaling of device dimensions has led to the current dielectric thickness of about 2-nm. However, leakage currents have been found to affect the performance of devices negatively[1].
Likewise, an oxide layer this thin is a low barrier against dopant diffusion. By replacing the SiO_2 with a higher dielectric constant material, the expected capacitance can be accomplished with a thicker layer, thereby reducing the leakage currents. The scaling towards higher cell densities can thus subsequently be achieved. Currently, thermally grown amorphous SiO_2 is used in microelectronic devices due to its high stability, quality interface with silicon, and higher electrical isolation properties[2].

The criterion for developing gate dielectrics such as homogeneous structures, large bandgap, high dielectric strength, and stable electrical characteristics makes silicon dioxide a reasonable candidate for practical applications. Various materials have many characteristics that are vital for replacing SiO_2, but very few are considered promising and fulfill all requirements. Materials that have shown some potential are Ta_2O_5, $SrTiO_3$, TiO_2, Al_2O_3, ZrO_2 and HfO_2. Among these, Ta_2O_5, $SrTiO_3$, TiO_2 have the highest dielectric constants, between 25 and 80 in thin films, but are not stable in contact with silicon. Reaction at the interface between film and substrate during the deposition experiment or subsequent heat treatment may lead to the formation of silicon oxide or silicides that is unfavorable to the electrical properties [3]. Ta_2O_5 and $SrTiO_3$ are still considered for memory applications.

However, TiO_2 is generally described as having a high leakage current, making it not convenient to use in its pure form. Moreover, the integration of the $SrTiO_3$ due to "polar catastrophe"[4] presents a greater challenge than that of the binary Ta_2O_5 and TiO_2. In addition to this, Al_2O_3, ZrO_2 and HfO_2 are thermodynamically stable in contact with silicon [5]. If an interfacial reaction occurs, the outcome will probably be silicates, which show moderate dielectric constants and may even be advantageous for the leakage characteristics. The dielectric constant of Al_2O_3 is only 8-10, and substituting SiO_2 with Al_2O_3 would thus only be a temporary solution. ZrO_2 and HfO_2, Moreover, their structure-modified derivatives (e.g., Zr and Hf silicates) have arisen as significant candidates for this reason since they have much higher dielectric constants than SiO_2 have dielectric constants of around 20 and offer more long-term solutions[6][7].

Ferroelectricity

Ferroelectricity is also one of the most important properties for manipulating and working microelectronic devices. In the early 1950s, the concept of memory using the ferroelectric property was published [8][9]. Ferroelectricity has been studied for application in electronics, such as the nonvolatile semiconductor device. Ferroelectric materials offer an extensive range of valuable properties for the electronic engineer to exploit, like insulating materials that form dielectrics; in other words, materials that will sustain a dielectric polarization under the application of an electric field.

Ferroelectricity is the material property of having spontaneous polarization and reversible switching under an applied electrical field. The polarization induced by the ferroelectric dipole is retained even after external power is cut off, and the external electrical field is zero. Various classes of ferroelectric materials exist with various technological applications, such as perovskite oxides.

Furthermore, ferroelectric materials are considered the most crucial electro ceramic materials because of their outstanding dielectric properties and electromechanical responses [10]. Therefore, perovskite-type ferroelectrics-related materials are interested in both the industrial and scientific fields. However, it is widely recognized that perovskite materials reduce ferroelectricity while decreasing particle size or film thickness. This severe issue makes it difficult to process them into integrated devices [11–13].

Part II

Motivation

Hafnia

The perovskite-type ferroelectrics and related materials are of great interest due to their excellent dielectric properties and electrochemical responses [10]. But it is widely recognized that perovskite materials show deterioration with downsizing, decreasing particle size, or film thickness. This problem makes it not practical to process them into integrated devices [11]. It has been reported that the perovskite-type ferroelectrics are incompatible with semiconductor technologies, so it is a reason for limited applications of ferroelectric thin films are reported[14]. HfO_2 ferroelectric materials have been reported by *Böscke et al.* [15] The most extraordinary attributes of these materials are that they have a simple chemical composition and thermodynamic stability, makes them highly compatible with various technological applications like Si-based semiconductor technology [16][17]. Ferroelectricity has been discovered in HfO_2 and ZrO_2 based high-k materials, [15] and these materials are of great interest due to their potential applications. It has been reported that HfO_2 based materials are employed as dielectric layers instead of conventional silicon oxides layers in current field-effect transistors due to their higher dielectric constant.[18, 19] Several intensive studies of ferroelectric devices for both capacitor-type ferroelectric memories and ferroelectric field-effect transistors have been reported [20]. However, specific applications such as ferroelectric tunnel junctions,[21] tunable capacitors,[17] and use in energy storage devices have been reported[22].

Zirconia

Furthermore, Zirconia (ZrO_2) also has extensive technological importance due to its exceptional mechanical and electronic properties, the dielectric constant, and large bandgap. It is reported as used in refractory, intricate ceramics, fuel cells, optical coating, catalytic agents, etc [23]. Due to its wide bandgap, and good thermal stability, it also has the potential to replace SiO_2 in advanced metal oxide semiconductor devices (MOS), memory devices, and optical applications [3]. Besides the above applications, it has been shown to have possible applications in capacitors, and metal-oxide-semiconductor (CMOS) technology is one of the most promising high constant dielectric materials. Overall, it can be said that ZrO_2 and HfO_2 can also be used as scaffold material to prevent leakage current through grain boundaries [24–26]. These twin oxides are being investigated due to their significant industrial and technological applications. Various works have been performed experimentally and theoretically to modify the bandgap by multiple means like doping and increase their effectiveness. Still, much room is available for further optimization of these oxides. Furthermore, as the ability to get crystalize, these materials have received prevalent attention in research, so investigation of mechanical properties is also as necessary as electronic and optical properties [27]. To the best of our knowledge, a thorough comparative study of these binary oxides' structural, electronic, and mechanical properties still has room to perform. Further investigation of their structural phases and electronic and ferroelectric properties may provide some valuable information.

Part III

Objectives

The primary goal of this work is to describe the electronic properties of two oxides ZrO_2 and HfO_2 and investigate the ferroelectric properties such as spontaneous polarization. Also, in this work, the dielectric properties of the orthorhombic, monoclinic, and tetragonal hafnia and zirconia are meant to be studied in terms of electronic contribution. The structural, electronic, and ferroelectric properties must be explored within the density functional theory (DFT) framework. The results are compared with available earlier reported experimental and theoretical data. These theoretical findings shall be worthwhile in providing guidelines for further optimizing structures for potential applications.

The details of the structures under study are described in the next chapter. Then, in the final analysis, the obtained results are presented.

Chapter 1

Introduction

1.1 Structural properties

Zirconium (Zr) and hafnium (Hf) are the transition metals resent in the 4-B of the periodic table, having atomic numbers 40 and 72, respectively. Generally, these metals form compounds having a hexagonal close-packed structure, with the most common oxidation state being +4. The size of oxides formed by these metals decreases down the group, but due to lanthanide contraction, zirconium and hafnium have an almost similar atomic size. Under their similar atomic properties, Zr and Hf show similar electronic and chemical bonding nature[28].

Hafnia (HfO_2) and zirconia (ZrO_2) exhibit many promising physical; and chemical properties. ZrO_2 is surprisingly similar to HfO_2 in many physical and chemical properties. As the temperature increases, both oxides exhibit multiple crystalline phases at ambient pressure, i.e., monoclinic, tetragonal, and cubic. One more outcome because of the almost similar chemical natures of the Hf and Zr atoms is that bulk hafnia and zirconia are shown to have similar crystal phases and phase diagrams[29].

1.1.1 Bulk Phases of HfO_2 and ZrO_2

The two twin oxides can adopt a variety of crystalline phases. Increasing the temperature, the monoclinic phase (m-phase-space group $P2_1/c$) transforms (between 1270 K and 1370 K for ZrO_2 [30] and at about 2073 K for HfO_2 [30, 31] into a tetragonal phase ($P4_2/nmc$) and further (at about 2650 K for ZrO_2 [23] and about 2900 K for HfO_2 [31] into a cubic phase (Fm3m). In addition, orthorhombic phases exist as an orthorhombic I phase (O-phase-Pbca), an orthorhombic II phase (OII-phase-Pnma), and a polar orthorhombic III phase ($Pca2_1$). The mono and ortho phases have 12 atoms and for tetragonal has six atoms in primitive crystal for both HfO_2 and ZrO_2.

Monoclinic

The chemical-physical properties depend hugely on the specific phase and structure. At ambient pressure and temperature, the monoclinic phase is the most stable form for ZrO_2 (space group $P2_1/c$) and HfO_2 (space group $P2_1/c$)). In the monoclinic phase ($a \neq b \neq c$) and ($\beta \neq 90°$), oxygen atoms can be either three or fourfold-coordinated, while the Hf atoms can be seven- or eightfold-coordinated. In ZrO_2 and HfO_2, there are 12 ion structures with four formula units where cation is surrounded by seven O atoms having two oxygen sites O_I and O_{II} in Wyckoff position 4e.

Tetragonal

The tetragonal structures of twin oxides have space group $P4_2/nmc$. The primitive unit cell for the tetragonal phase for both oxides is composed of two cations, Hf, Zr ($a = b \neq c$) and ($\beta = 90°$). The Hf/Zr and O are in Wyckoff positions 2(3/4,1/4,3/4) and 4d(1 / 4, 1 / 4, z), respectively.

Orthorhombic

Another significant phase of ZrO_2 and HfO_2 is the orthorhombic phase, as this phase is reported to have spontaneous polarization. Usually, for this oxide, two sorts of orthorhombic phases exist. One orthorhombic structure (Ortho-I) has space group Pbca, while the other orthorhombic phase (Ortho-II) has space group Pnma, and the last orthorhombic phase (Ortho-III) has space group $Pca2_1$. The structure understudy for this project is Ortho-I. The primitive cell consists of 12 ions while Hf/Zr is surrounded by O and O_{II} having Wyckoff position 8c.

Chapter 2

DFT

2.1 Introduction

Density functional theory (DFT) is the successful quantum mechanical approach to investigating the electronic structures of many-body systems in the ground state [32]. It is based upon a simple computational method, which has become the most helpful tool in first-principle calculations to determine the properties of molecular and condensed matter systems.

2.2 Quantum many-body Equation

In quantum mechanics,s all the information about the system can be obtained from the wave function. To solve any system,m is just the eigenvalue equation.[33]

$$\hat{H}\Psi = E\Psi \tag{2.1}$$

Is required. But the potential external properties of the whole system are not as simple [34]. In the case of a single body problem, the observables remain independent of the motion of particles and their positions in the system. Meanwhile, the interaction of particles in the system and the variation make the system complex for analysis. In the case of any solid where electrons interact with themselves and ion cores that form the crystal structure makes, these systems are complicated.

Different approximations have been developed to deal with complex systems and simplify calculations. In this respect, DFT is one of the best methods to calculate the properties of the many-particle system,s such as conductivity, binding energy, and polarizability. With the help of current approximations, it is easy to handle complex many-body interacting systems. The interacting system is taken as a non-interacting system to find the properties of a system. In short, it describes an interacting system by the density of fermions rather than by its many-body wave functions. The density must be known to calculate the ground-state properties of complex systems using the DFT. Here, the electron density is observable,e, a function of three variables x, y, and z, unlike the wave function consisting of 3N variables for N electron systems. By determining the charge density of any particular system, the whole system can be characterized; the number of calculations could be reduced. DFT uses the charge density to describe the system of interacting particles under the influence of external potential $V_{ext}(\vec{r})$.

In an interacting system there is a collection of positively charged nuclei and negatively charged electrons. Which is the situation of many body problem having N+ZN particles, where N and ZN corresponds to number of nuclei and electrons in the system, respectively. The Hamiltonian for the respective system can be written as,

$$\hat{H} = \frac{-\hbar}{2}\sum_i\left(\frac{\nabla_{R_i}}{M_i}\right) - \frac{-\hbar}{2}\sum_i\left(\frac{\nabla^2_{r_i}}{m_e}\right) - \sum_i\sum_j\frac{e^2}{4\pi\epsilon_0}\frac{Z_i}{|\vec{R_i}-\vec{r_j}|} + \sum_i\sum_{j\neq i}\frac{e^2}{8\pi\epsilon_0}\frac{}{|\vec{r_i}-\vec{r_j}|} + \sum_i\sum_{j\neq i}\frac{e^2}{8\pi\epsilon_0}\frac{Z_iZ_j}{|\vec{R_i}-\vec{R_j}|} \quad (2.2)$$

Here, M_i is the mass of a heavier particle (nucleus,) and m_e is the mass of the lighter particle (electron). In the above equation, the first two terms refer to the kinetic energy operators for the nucleus and electrons, respectively. The third term represents the potential energy between the electrons and nuclei

– the total electron-nucleus coulombic attraction in the system. The fourth term represents the potential energy arising from coulombic electron-electron repulsion, and the last term is the potential energy arising from coulombic nuclei-nuclei repulsions – also known as the nuclear repulsion energy.

2.3 Approximations

most complex systems Hamiltonian could not be solved simply. Exact solutions of Schrödinger equations exist only for a few idealized systems. Hence, for complex systems, approximations are needed. Several approximations have been made to the time to solve the complex problem,s, e.g., perturbation theory by Dirac, the variational method by Hayllerass and WKB(Wentzel-Kramers-Brillouin) method are common examples. Depending upon the Hamiltonian of the system to solve the eigenvalue problem, the above approximation methods are primarily used.

The perturbation theory is employed where approximated solutions are required based on the exact answer. In this case, the perturbed Hamiltonian is solved separately from the solvable Hamiltonian in the results are added as correction energy in the total solution. For such systems where Hamiltonians can not be reduced to precisely solvable Hamiltonians,s and by adding minor correction, another widely-used approximation is the WKB-method (Wentzel-Kramers-Brillouin), a variational principle.[3] Usually, WKB-method is regarded as the semi-classical approximation because it applies to classical systems for which it is approximate,d the potential is considered to remain constant over a region of de-Broglie wavelength. The variational principle is used to calculate the ground state energy of the system without solving the Schrodinger wave equation.

2.3.1 The Born-Oppenheimer Approximation

In this approximation, nuclei are considered to be at rest as they are much heavier than electrons, so the kinetic energy of the nucleus is zero,o and the nuclei's potential term becomes constant [4]. After implementation of this approximation, the total Hamiltonian term reduces to

$$\hat{H}_{tot} = \hat{T}_e + \hat{V}_{ee} + \hat{V}_{ext} \tag{2.3}$$

$$\hat{H}_{tot} = \frac{-\hbar}{2m_e}\sum_{i=1}^{N}\nabla_i^2 + \frac{1}{2}\sum_{i}^{N}\sum_{i\neq j}\frac{1}{|\vec{r_i} - \vec{r_j}|} - \frac{1}{2}\sum_{i}^{N}\sum_{i\neq j}\frac{Z_i - Z_j}{|\vec{r_i} - \vec{r_j}|} \tag{2.4}$$

Here, the first term shows the kinetic energy operator of the electrons, while the other two terms are electron-electron and electron-nuclei coulombic interaction,s respectively [5]. This approximation shapes the Hamiltonian into a much simpler form.

2.3.2 Hartree Approximation

To solve the many-body problem, the first method was introduced by Hartree. The concepts of the mean-field theory were utilized. To solve the many-body problem and bring many-body systems to the approximated one body system [6]. The simplest approximation of the wavefunction for the many-electron Schrödinger equation is to assume that electrons act like independent electrons. The wavefunction with N independent electrons can be written as then,

$$\Psi(\vec{r_i}) = \psi(\vec{r_1}, \psi(\vec{r_2})\psi(\vec{r_3}), \ldots, \psi(\vec{r_N}) \tag{2.5}$$

Here, $\psi(\vec{r_i})$ is the wave function of ith electron, and atoms are considered as fixed in their positions, so, subsequently, the R_i are suppressed in the wavefunction. The energy of the many-electron system within the Hartree approximation can be written as

$$E = \langle \Psi(\vec{r_i})\hat{H}\Psi(\vec{r_i})\rangle \tag{2.6}$$

Applying the hartree approximation to this hamiltonian, the Schrodinger wave equation, is of the form:

$$\hat{H} = \sum_{i=1}^{N} \hat{H}_i + \frac{1}{2}\sum_{i \neq j}^{N} V_{ij} \tag{2.7}$$

The problem with this theory was the violation of conditions of the anti-symmetric wave function because the Pauli exclusion principle was ignored. Later this theory was improved by Fock by considering the anti-symmetric wave functions [7]. From the Hartree approximation, the ground states can be achieved,d and the many-electron equation becomes N single-electron equations.

2.3.3 Hartree-Fock approximation

Hartree-Fock (HF) approximation is a method that considers antisymmetry of the wave function. Slater introduced a way to construct such a wave function[35]. The wave function of the many-electron Schrödinger equation is described in the form of a matrix determinant for the N electrons, which is defined as

$$\Psi(\vec{r_1}, \vec{r_2}, \ldots, \vec{r_N}) = \frac{1}{\sqrt{N!}} \begin{vmatrix} \psi_1(\vec{r_1}) & \psi_2(\vec{r_1}) & \ldots & \psi_N(\vec{r_1}) \\ \psi_1(\vec{r_2}) & \psi_2(\vec{r_2}) & \ldots & \psi_N(\vec{r_2}) \\ \vdots & \vdots & & \vdots \\ \psi_1(\vec{r_N}) & \psi_2(\vec{r_N}) & \ldots & \psi_N(\vec{r_N}) \end{vmatrix} \tag{2.8}$$

In the above equation, $\frac{1}{\sqrt{N!}}$ is the normalization constant, and $\psi_i(\vec{r_i})$ is the wave function of the i-th electron according to Pauli's exclusion principle, this relation of wave functions describes the anti-symmetric nature of fermions, and particles are indistinguishable. Utilizing the determinant for wave function,s the product of the spin-wave function is given as:

$$\psi_i(\vec{r_i}, \sigma_i) = \phi(\vec{r_i})\chi(\sigma_i) \tag{2.9}$$

In general, the HF method allows the electron to move in the approximated mean-field and nuclear potential,l which is often termed external potential,l which is acted upon by the system's particles. This potential is usually estimated as the effective potential. Somehow this theory provides a qualitative approach to many materials,s but it is incapable of a quantitative approach.

2.3.4 Density Functional Theory

To solve the many-electron Schrödinger equation, the Hartree and HF methods are traditional, but the HF method only includes the exchange term and not the electron correlation term. This makes them unsuitable for solid materials. In addition to the Hartree and HF methods, there is a modern method to solve the more complicated calculations of many-electron systems, namely the density functional theory (DFT). It was introduced by Hohenberg and Kohn in 1964 [36], and Kohn became practical in the mid-1980s. In 1998, Kohn and Pople were awarded the Nobel Prize in Chemistry for developing DFT and computational methods in quantum chemistry, respectively. The idea of the DFT is to consider the electron density in solid materials instead of using the many-electron wave function. Using this,s the degree of freedom reduces from 3N (N is the number of electrons) to 3. Thereby it simplifies the calculations.

The density as the primary variable

Considering the electron density as a wave function,n can have two consequences. The first one is in a many-electron system to describe the relationship between electron density and wave function. The second one is how to solve the problem if considering the electron density instead of the wave function. These problems can be explained with the help of two theorems introduced by Hohenberg and Kohn [36][37].

Theorem 1

The external potential $V_{ext}(\vec{r})$ is determined uniquely for any many-electron system by the ground-state electron density ρ.

According to the above theorem, it is indicated that all ground-state properties can be determined by the ground state density ρ_o.For instance, the total ground-state energy $E = E[\rho_o]$ where, $\rho_o(\vec{r}) = |\Psi_o(\vec{r})|^2$. The theorem suggests that the external potential can be obtained if the ground-state electron density is known. Thus the Hamiltonian is known for the external potential. The corresponding wave function is determined from which electron density can be calculated. Moreover, the external potential is uniquely determined by the electron density. Hence all ground-state properties are determined uniquely from the electron density. To prove this: assume that there exits two potentials $V_{ext}(\vec{r})$ and $V_{ext}\prime(\vec{r})$ leads to the same ground-state density, so it will have two Hamiltonian H and H′ which corresponds to two wave functions Ψ and Ψ'. these lead to the following equation

$$E = \langle\Psi|H|\Psi\rangle < \langle\Psi'|H|\Psi'\rangle, \quad \text{and} \quad E' = \langle\Psi'|H'|\Psi'\rangle < \langle\Psi|H'|\Psi\rangle \tag{2.10}$$

using 2.4 and 2.10 following relation can be derived

$$E < E' + \int (V_{ext}(\vec{r}) - V'_{ext}(\vec{r})\rho(\vec{r})d\vec{r}) \tag{2.11}$$

and analogous relation can be derived for $\langle\Psi|H'|\Psi\rangle$

$$E' < E + \int (V'_{ext}(\vec{r}) - V_{ext}(\vec{r})\rho(\vec{r})d\vec{r}) \tag{2.12}$$

form 2.3.4 and 2.12

$$E + E' < E' + E \tag{2.13}$$

Which implies the significance of the uniqueness of V_{ext}.

Theorem 2

There is a universal functional $F[\rho]$ for the total energy in the terms of the electron density ρ with any external potential $V_{ext}(\vec{r})$, and the exact ground-state density is obtained when the ground-state total energy functional reaches its minimal value, that is, $E[\rho'] > E[\rho]$. Here, ρ_o is the exact ground-state density.

The first theorem implies that the kinetic and interaction energies are functionals of electron density. The total energy can be expressed in the following way (ignoring the interaction between nuclei)

$$E[\rho] = \langle\Psi|V_e + V_{int} + V_{ext}|\Psi\rangle$$

$$= \langle\Psi|V_{ext}(\vec{r})|\Psi\rangle + \langle\Psi|V_e + V_{int}|\Psi\rangle \tag{2.14}$$

$$E = \int \rho(\vec{r})V_{ext}(\vec{r})d\vec{r} + F[\rho]$$

In the many-electron system,m $F[\rho]$is universally functional in the above equation. At exact ground state density ρ, the functional of total energy $E[\rho']$ reaches the minimum. Here, the total energy for the case of exact ground-state electron density is smaller than in any other case. Therefore, the exact ground-state electron density can be achieved by minimizing the total energy.

2.3.5 Kohn-Sham Equations

According to the Kohen and Hohenberg theorems, the ground state density contains all information about the physical properties of the systems as a wave function. But they could not determine the respective ground state density for the systems. Later in 196,5, Kohn and Sham preceded the sets of equations known as the Kohn-Sham Equation[38]. With the exact ground state energy for two systems, the system of interacting electrons follows the auxiliary system of non-interacting electrons. The KS (Kohn-Sham)equation is a method to solve the many-electron Schrödinger equation exactly while using an incorrect simplified wavefunction, typically chosen as a Hartree-like wave function. Assume that the Hartree-like wave function obtains the exact ground-state density. The electron density is defined as:

$$\rho(\vec{r}) = \sum_{i}^{n} \psi_i^{KS*}(\vec{r})\psi_i^{KS}(\vec{r}) \tag{2.15}$$

Here, n is the number of electrons, and $\psi_i^{KS}(\vec{r_i})$ is an auxiliary independent single-electron wave function. If the electron density is exact the total energy is exact which can be stated as:

$$\begin{gathered} E[\rho] = T[\rho] + V_{int}[\rho] + V_{ext}[\rho] \\ = T_0[\rho] + V_H[\rho] + V_{ext}[\rho] + (T[\rho] - T_0[\rho]) + (V_{int}[\rho] - V_H[\rho]) \\ = T_0[\rho] + V_H[\rho] + V_{ext}[\rho] + E_{xc}[\rho]. \end{gathered} \tag{2.16}$$

In 2.16 $E[\rho]$ is the total energy, and ρ is the ground-state density. $T[\rho], V_{int}[\rho], and V_{ext}[\rho]$ represent energies from the exact kinetic, the exact electron-electron interaction, and external potential, respectively. $E_{xc}[\rho]$ is called the exchange-correlation energy. The $T_0[\rho]$, $V_H[\rho]$, and $V_ext[\rho]$ represent the kinetic energy in the Hartree approximation, the electron interaction energy in the Hartree approximation, and the electron-nuclei interaction energy, respectively. Moreover, the term $V_H[\rho]$ includes the self-interaction and electron,s thereby allow to interact with themselves. It is widespread to write in this way for many-electron problems.

To derive the ground-state properties in the many-electron system, one can view this problem as the process of minimizing the total energy by varying the wave function $\psi_i^{KS*}(\vec{r})$ such as;

$$\frac{\delta}{\delta\psi_i^{KS*}(\vec{r})}\left(E[\rho] - \sum_{i}^{N}\sum_{j}^{N} E_{i,j}^{KS}\left(\langle\psi_i^{KS}(\vec{r_i})\psi_i^{KS}(\vec{r_j})\rangle\right)\right) \tag{2.17}$$

using the variational principle, the KS equation can be derived as;

$$H\psi_i^{KS}(\vec{r}) = \left(\frac{-\hbar^2\nabla^2}{2m} + V^{KS}(\vec{r})\right)\psi_i^{KS}(\vec{r}) = \varepsilon_i^{KS}\psi_i^{KS}(\vec{r}) \tag{2.18}$$

and

$$V^{KS}(\vec{r}) = V_{ext}(\vec{r}) + \int \frac{\rho(\vec{r'})}{|\vec{r}-\vec{r'}|}d\vec{r'} + \frac{\delta E_{XC}}{\delta\rho(\vec{r})} = V_{ext}(\vec{r}) + \int \frac{\rho(\vec{r'})}{|\vec{r}-\vec{r'}|}d\vec{r'} + V_{XC}(\vec{r}) \tag{2.19}$$

KS equation is equal to the Hartree equation and derived in similar manner if $V_{XC}\vec{r} = 0$ and $\Psi^{KS}\{r_i\} = \Psi^{HF}\{r_i\}$, and $V_{XC}\vec{r}$ is have only exchange potential then Kohn-Sham equation will be equal to Hartree Fock equation. The total energy expression is given below:

$$E[\rho] = \sum_{i}^{N} -\frac{1}{2}\int\int \frac{\rho(\vec{r'})\rho(\vec{r})}{|\vec{r}-\vec{r'}|}d\vec{r}d\vec{r'} + E_{XC}[\rho] - \int V_{XC}(\vec{r})\rho(\vec{r})d\vec{r} \tag{2.20}$$

In the KS equation, the auxiliary independent single-electron wave function in the KS equation is not an exact single electron wave function. However, the exact ground-state density may be calculated using the auxiliary wave function. Therefore, the KS equation is exact only if the $V_{KS}(\vec{r})$ is exact[39].

2.3.6 Exchange-correlation potential

The most challenging part of solving the KS equation is the exchange-correlation potential because the exact form is still unknown today. Therefore, there are various approximations, such as the local density approximation (LDA) [33, 40], a generalized gradient approximation (GGA) [39, 41–43].

Local density approximation

The local density approximation (LDA) is an approximation and a simple way to approximate the exchange-correlation part[44]. Which is based on the free homogeneous electron gas theory, which has a constant electron density. This scheme assumes that many-body electron systems are uniformly distributed, having a constant density remaining in the same system. In the LDA, then it is considered that the exchange-correlation energy for an electron in a very minute small volume in a many-particle system is equal to the exchange-correlation for an electron in the free electron gas with the same density as in the volume for this analytical approximation for exchange-correlation functional within the density of the system is given as,

$$E_{XC}^{LDA}[\rho] = \int \rho(\vec{r})\varepsilon_{XC}^{gas}(\rho(\vec{r})d\vec{r} \tag{2.21}$$

and compatible exchange-correlation potential can be written as,

$$V_{XC}^{LDA}(\vec{r}) = \frac{\delta E_{XC}^{LDA}[\rho]}{\delta\rho}$$

Somewhat the LDA could be pretty accurate for solids. This is mainly due to a cancellation of errors between the exchange and correlation parts since it fulfills the sum rule for the so-called XC-hole [45]. HOWEVER, the LDA tends to over-bind solids, resulting in somewhat underestimated lattice constants and overestimated bulk moduli [46].

Generalized Gradient Approximation

The LDA does not generate good accurate results for the more modified systems where electron density does not vary slowly. The generalized gradient approximation (GGA) is used to solve this issue. This approximation uses both the exchange-correlation functional as function of density and gradients of density $|\nabla\rho(\vec{r})|$. The outcomes obtained from GGA were proved to be better in many cases than the LDA and other approximations. It provides satisfactory results for the total energy of the systems, binding energies, ground-state properties of many compounds, and structural optimizations [44]. The mathematical representation of GGA is given as,

$$E_{XC}^{GGA}[\rho] = \int \rho(\vec{r})\varepsilon_{XC}^{GGA}(\rho(\vec{r}, \nabla\rho(\vec{r}))d\vec{r}$$

As the GGA can not be derived uniquely, there are many variants of GGA functionals, varying in implementing the gradient component. A different approach is to design functional forms to make $\varepsilon_{XC}^{GGA}(\rho(\vec{r}, \nabla\rho(\vec{r}))$ satisfy a set of properties (typically certain constraints and limiting behaviors) known to be obeyed by the exact XC functional. Well-known examples along this route are the Perdew-Wang91 [47], the Perdew-Burke-Ernzerhof (PBE), [48] and the PBEsol [49]. The GGA functional used in this work has been a variant of the (PBE) functional. The PBE form is the most widely used GGA.

DFT+U

The LDA and GGA will often fail to accurately describe electron states that are strongly localized, typically d or f-like states. This is primarily maybe due phenomenon of the self-interaction of the KS particles in the LDA/GGA description, i.e., that the KS particles feel repulsion from their presence. There are many approaches in use to attempt to resolve this issue. One of them is taking inspiration from the well-studied Hubbard model. One common way is by augmenting the DFT description with an on-site, Hubbard-like term. The total modified energy with new insertion can be written as,

$$E_{DFT+U}[\rho] = E_{DFT}[\rho] + E_{Hubbard}\left[\{n^{I,\sigma}_{m,m\prime}\}\right] - E_{DC}\left[\{n^{I,\sigma}\}\right] \tag{2.22}$$

where, $E_{Hubbard}\left[\{n^{I,\sigma}_{m,m\prime}\}\right]$, is the Hubbard-like on-site term and $E_{DC}\left[\{n^{I,\sigma}\}\right]$ is a "double counting" term, which is needed since $E_{DFT}[\rho]$ already describes part of the energy that is added in $E_{Hubbard}\left[\{n^{I,\sigma}_{m,m\prime}\}\right]$. $\left[\{n^{I,\sigma}_{m,m\prime}\}\right]$ is on site occupation matrix such as;

$$n^{I,\sigma}_{m,m\prime} = \sum_{i}^{occ.} \langle \psi^{\sigma}_{i} | \phi^{I,\sigma}_{m} \rangle \langle \psi^{\sigma}_{i} | \phi^{I,\sigma}_{m'} \rangle, \tag{2.23}$$

with ψ^{KS}_{i} are the KS-orbitals, $\phi^{I,\sigma}_{m}$ localized (typically d- or f-)orbtials at atomic site I and σ the spin-index. Many other various forms exist for both $E_{Hubbard}$ and E_{DC}. A popular variant is that of Dudarev *et al.*[50] where the energy takes the form like that:

$$E_{DFT+U}[\rho] = E_{DFT}[\rho] + \frac{U-J}{2} \sum_{I,\sigma} \left(\sum_{m} n^{I,\sigma}_{m,m} - \sum_{m,m'} n^{I,\sigma}_{m',m} n^{I,\sigma}_{m,m'} \right)$$

Here, U and J can not be used separately. Only the value of $U_{eff} = U - J$ is of importance. The "J" parameter is the exchange interaction term that accounts for Hund's rule coupling. The U_{eff} is generally preferred because the J parameter is proven crucial to describing the electronic structure of certain classes of materials, typically those subject to strong spin-orbit coupling. To do so, values of U and J or U_{eff} should be chosen, and some results may depend sensitively on the value of U. In principle, methods exist to determine them from the first principle [51]. Still, they are often chosen to match results from higher-order theory or the experiment in practice.

The U correction's fundamental role is to treat the solid on-site Coulomb interaction of localized electrons with an additional Hubbard-like term. The Hubbard Hamiltonian describes the strongly correlated electronic states (d and f orbitals) while treating the rest of the valence electrons by the normal DFT approximations.

2.3.7 Electronic density of states

Several physical quantities can be calculated once DFT calculations are completed to run. The electronic density of states (DOS for the present work) is a calculation of great importance [52]. Electronic DOS is used, e.g., to classify the bulk material and estimate electronic properties such as bandgap properties. In addition, the energy density of states $D(\epsilon)$ is helpful when dealing with sums over functions, such as $F(\epsilon_k)$, which depend on the k-states that act through an energy function ϵ_k such as:

$$\sum_{k,\sigma} F(\epsilon_k) = \nu \int d\epsilon D(\epsilon) F(\epsilon) \tag{2.24}$$

In the above equation ν is regarded as the volume of the material and the Pauli exclusion principle allows two electrons with opposite spins (σ) to be present for each k-point. $\frac{2}{\nu} \sum_k = \int dk$ can be used to calculate D(ϵ), the relationship between the summation and integration of density of states is given as:

$$\begin{aligned}\textstyle\sum_{k,\sigma} F(\epsilon_k) &= \nu \textstyle\int [dk] F(\epsilon) \\ &= \nu \textstyle\int d\epsilon \textstyle\int [dk] \delta(\epsilon - \epsilon_k) F(\epsilon)\end{aligned} \tag{2.25}$$

A value of unity with integrating the δ function concerning ϵ.The integration 2.24 was done concerning k, then 2.24 is compared to 2.25 so, the $D(\epsilon)$ can be written as:

$$D(\epsilon) = \int [dk] \delta(\epsilon - \epsilon_k)$$

The density of states (DOS) of a system describes the proportion of states that are occupied by the system at each energy. The density of states is defined as $D(E) = N(E)/V$, where $N(E)dE$ is the number of states in the system of volume V whose energies lie in the range from E to $E + dE$.

The electronic DOS analyzes the bulk material by dealing with the bandgap located between the valence and conduction bands in insulators and semiconductor materials. The material is claimed to be metal if it has no bandgap. Unfortunately, the bandgap in LDA/GGA calculations is typically underestimated [98, 99], and several correction methods for this problem have, in some instances, been achieved as well as utilized described in, e.g. [100].

Local density of states

To interpret the structure of material ultimately, a description of actual states in the domain of specific atoms is quite a handful. A common way of finding this is by calculating the local density of states (LDOS). The LDOS can be explained as the number of electronic states at specific energy that appears in a specified volume around the nuclei. LDOS can be split into the specific partial density of states (PDOS) due to an element's s, p, and d-orbitals.

2.4 Computational Details

In this project, density theory calculations have been performed using the Vienna ab initio simulation package (VASP) [53–55], which performs a variational solution of the Kohn–Sham equations in a plane-wave basis set. Electronic exchange and correlation are described in the generalized gradient approximation, using the functional proposed by Perdew–Burke–Ernzerhof (PBE) [56]. The input parameters in these calculations are only the atomic number and atomic positions in the unit cell of the considered material. For the plane-wave set, cutoff energy of 600 eV for structural relaxation is used. The k-point meshes in the full wedge of the Brillouin zone (BZ) are sampled by $10 \times 10 \times 10$ grids according to the Monkhorst-Pack [57]. The hafnium $5p^6$ $6s^1$ $5d^3$ and for oxygen $2s^2$ $2p^4$ electrons are treated as valence electrons. The strong on-site Coulomb repulsion among the localized Hf 5d electrons is described by using the formalism developed by Dudarev *et al.*[50] .

Chapter 3

Results and Discussion

3.1 Structural Optimization

The optimized structures of monoclinic (mono) and orthorhombic (ortho) phases of twin oxides are represented in Fig 3.1 and 3.2 respectively. The monoclinic and ortho ($Pca2_1$) phases of MO_2 (M = Hf and Zr) have seven-fold cation coordination (there are seven oxygen atoms around each M atom) and two different oxygen sites O_I and O_{II} (O_I atom is coordinated to three M atoms in an almost planar environment, and O_{II} atom is surrounded by a distorted tetrahedron of four M atoms).

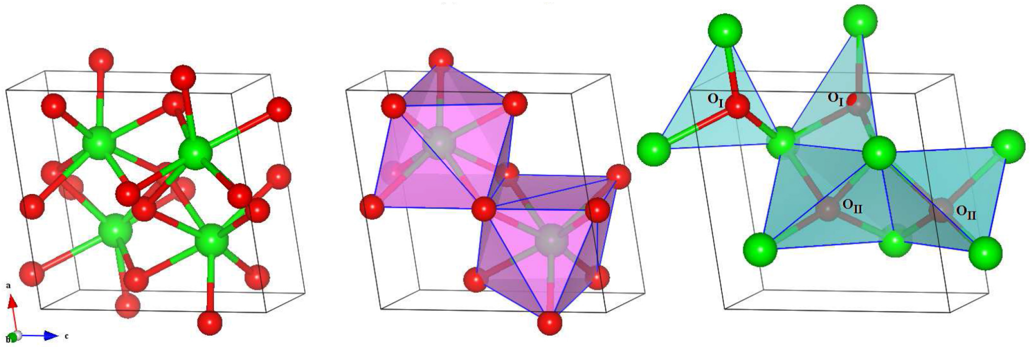

Figure 3.1: Optimized monoclinic crystal structure for MO_2 (M = Hf and Zr). The green and red balls represent cation M and O atoms, respectively [58].

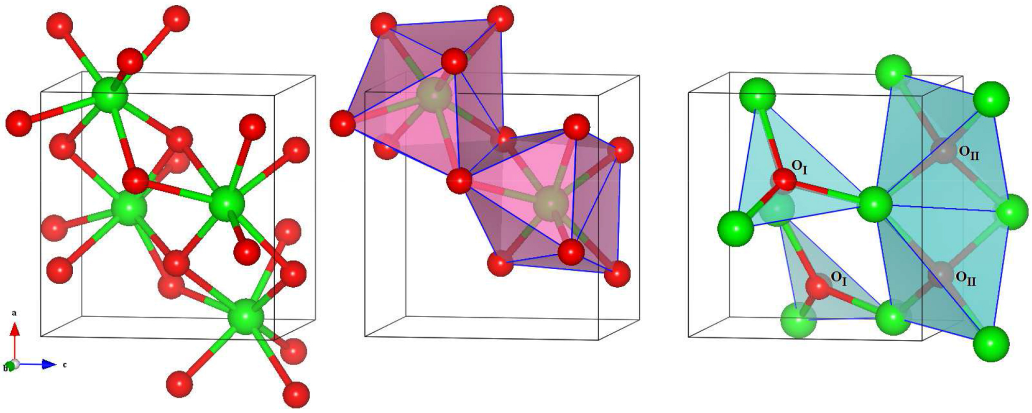

Figure 3.2: Optimized crystal structure of orthorhombic MO_2 (M = Hf and Zr) .

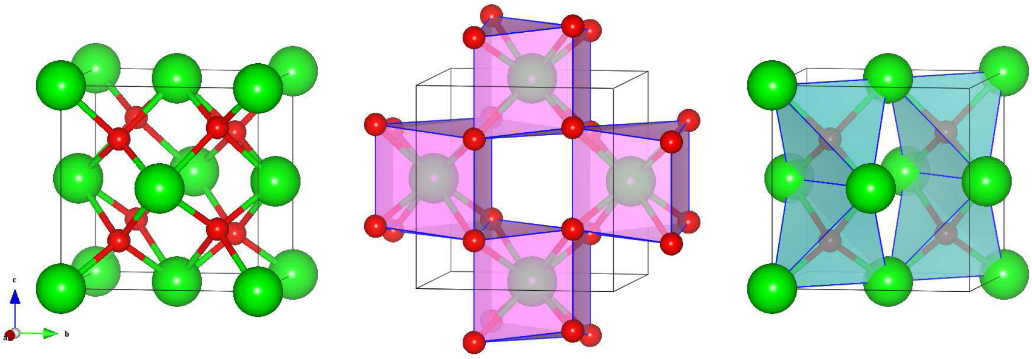

Figure 3.3: Optimized crystal structure of tetragonal MO_2 (M = Hf and Zr).

From the Fig. 3.3, it can seen that the tetragonal(tetra) MO_2 (M = Hf and Zr). It has been studied that this structure is derived from the cubic one by an increase of the c/a ratio from $\sqrt{2}$ for the perfect cube to 1.437 and there is an internal displacement of the oxygen atoms along the z-direction. These alternating columns of oxygen atoms are shifted upwards and downwards by an amount of z. Then the tetragonal MO_2 is characterized by the two lattice parameters along x-axis (a) and z-axis (c) and the third one, the internal parameter d_z related to this displacement of the oxygen atoms by $d_z = \Delta/c$. The Zr cation (O anion) is inside a distorted cubic (tetrahedron) tetragonal MO_2 has eight-fold cation coordination (there are eight oxygen atoms around each M atom) and an identical oxygen site. The Wyckoff positions for optimized structures are listed in Table. 3.1 and Table. 3.2 for zrO_2 and HfO_2 respectively.

Table 3.1: Wyckoff positions, cation and anion coordination of ZrO_2

Phases	Mono	Tetra	Ortho
Wyckoff	**Zr(4e)**	**Zr(2a)**	**Zr(4a)**
positions	x = 0.276	0	0.265
	y = 0.044	0	0.749
	z = 0.210	0	0.031
	O_{I}(4e)	**O(2d)**	**O_{I}(4a)**
	x = 0.066	0.5	0.0655
	y = 0.327	0	0.604
	z = 0.476	0.31 + 0.19	0.866
	O_{II}(4e)	**O(2d)**	**O_{II}(4e)**
	x = 0.549	0	0.465
	y = 0.743	0.5	0.0
	z = 0.523	0.69 - 0.19	0.2732
Cation	Zr(7-O)	Zr (8-O)	Zr(7-O)
Anion	O_{I}(3-Zr)	O (4-Zr)	O_{I}(3-Zr)
	O_{II}(4-Zr)	O	O_{II}(4-Zr)

Table 3.2: Wyckoff positions, cation, and anion coordination of HfO_2

Phases	Mono	Tetra	Ortho
Wyckoff	**Hf(4e)**	**Hf(2a)**	**Hf(4a)**
positions	x = 0.276	0	0.265
	y = 0.044	0	0.749
	z = 0.210	0	0.031
	O_I(4e)	**O(2d)**	**O_I(4a)**
	x = 0.066	0.5	0.0655
	y = 0.327	0	0.604
	z = 0.476	0.31 + 0.19	0.866
	O_{II}(4e)	**O(2d)**	**O_{II}(4e)**
	x = 0.549	0	0.465
	y = 0.743	0.5	0.000
	z = 0.523	0.69 - 0.19	0.273
Cation	Hf(7-O)	Hf (8-O)	Hf(7-O)
Anion	O_I(3-Zr)	O (4-Zr)	O_I(3-Zr)
	O_{II}(4-Zr)	O	O_{II}(4-Zr)

Bond lengths

For the monoclinic phase, the average bond lengths for Zr–O_I, Zr–O_{II} are observed to be 2.25 and 3.01 Å respectively. For Hf–O_I and Hf–O_{II} 2.21 and 2.01 Å respectively. Further, the estimated average distance between cations Zr–Zr and Hf–Hf bonds are 3.54 and 3.48 Å respectively. When structural relaxation using U = 3eV is employed, for both oxide the increase of 0.1 Å in values of bond lengths is observed.

Furthermore, the average bond lengths from the optimized structure of the orthorhombic phase approximated for Zr–Zr and Hf–Hf bonds are found to be 4.34 and 3.58 Å respectively. Also for Zr–O_I, Zr–O_{II} are detected to be 2.14 and 2.22 respectively. For Hf–O_I and Hf–O_{II} 2.11 and 2.19 Å respectively. Subsequently, for the tetragonal phase, the bond distance between Zr–Zr, and Hf–Hf is 3.70 and 3.64 Å. For Zr-O and Hf-O are 2.27 and 2.24 Å respectively.

3.1.1 Lattice parameters

Table 3.3: Calculated lattice parameters (a, b and c) for three phases HfO_2 are in Å and volume (in Å^3).

Phases	space group	experiment	Theoretical	PBE	PBE+U
Mono	$P2_1/c$	a = 5.12^b	5.14^a	5.14	5.20
		b = 5.17^b	5.19^a	5.19	5.23
		c = 5.29^b	5.32^a	5.33	5.29
		ν = 140.02	142.92	140.46	143.86
Ortho	$Pca2_1$	a = 5.23^d	5.29^c	5.05	5.10
		b = 5.23^d	5.01^c	5.08	5.13
		c = 5.05^d	5.08^c	5.27	5.30
		ν = 138.13	134.63	135.20	138.66
Tetra	$P4_2/nmc$	a = 3.40^f	3.13^e	3.10	3.62
		b = 3.40^f	3.14^e	3.60	3.62
		c = 5.29^f	5.24^e	5.22	5.19
		ν = 61.15	51.66	67.65	68.01

a[59, 60],b[61],c[62],d[63],e[29],f[64]

The lattice parameters of the HfO_2 and ZrO_2 unit cells of each phase under study are optimized under 0 K and stress-free conditions are listed in Table. 3.3 and 3.4 along with available experimental data and also previously reported theoretical values. The structural optimization is performed using total energy per unit cell versus the lattice parameters, and thus optimized lattice constants are computed.

It has been reported earlier that the accuracy of the calculated results depends on the chosen density functional and pseudo-potential. While lattice constants from GGA calculations are typically too large, the results from LDA calculations are typically too small (about 1 %). From the Table 3.3 and 3.4it is evident that some of the computed values in this work are in good agreement with the results reported from the experimental study and other theoretical works. Comparing HfO_2 and ZrO_2, it can be seen that the latter has a slightly bigger unit cell that can be observed from the reported values of volume of unit cells. That is consistent with the lanthanide contraction argument as described earlier. Zr and Hf have electronic configuration ($[Kr]4d^2 5s^2$) ($[Xe]4f^{14} 5d^2 6s^2$) respectively, occupies the same group of the periodic table, with the most similar electronic structure difference between them being that hafnium possesses a closed subshell of electrons and zirconium has no f-electrons. Also, due to ensuing lanthanide contraction, both the atomic and the ionic radii of these atoms are nearly the same[65].

Table 3.4: Calculated lattice parameters (a, b and c) for three phases ZrO_2 are in Å and volume (in Å^3).

Phases	space group	experiment	Theoratical	PBE	PBE+U
Mono	$P2_1/c$	a = 5.12[61]	5.13[28]	5.18	5.26
		b = 5.17[61]	5.19[28]	5.24	5.28
		c = 5.29[61]	5.30[28]	5.30	5.34
		ν =140.03	141.11	143.85	148.30
Ortho	$Pca2_1$	a=5.20[62]	5.23[63]	5.01	5.15
		b = 5.00[62]	5.03[63]	5.13	5.18
		c = 5.05[62]	5.06[63]	5.32	5.35
		ν =131.30	133.11	136.73	142.72
Tetra	$P4_2/nmc$	a = 3.64[64, 66]	3.57[29]	3.62	3.65
		b = 3.64[64, 66]	5.07[29]	3.62	3.65
		c = 5.27[64, 66]	5.20[29]	5.28	5.24
		ν =69.82	66.27	69.19	69.80

3.2 Dielectric Properties

A dielectric material is an insulator that can be polarized when an electric field is applied. When placed into an electric field, the material's internal structure becomes polarized, with the positive ions shifting towards the field and the negative ions moving in the opposite direction. This creates a charge difference across the whole material without the conductance of electrons.

A material's dielectric constant, k (the average value taken from the dielectric tensor matrix), also known as relative permittivity, indicates how easily an applied electric field polarizes it. k is a dimensionless ratio between the complex frequency-dependent absolute permittivity of the material $\epsilon(\omega)$, and permittivity of free space ϵ_0 while

$$k = \frac{\epsilon(\omega)}{\epsilon_0} \tag{3.1}$$

and k is related to electric susceptibility χ_e as.

$$k = 1 + \chi_e$$

The electric susceptibility is defined as the constant of proportionality which relates to the dielectric polarizability p induced by an electric field, E:

$$p = \epsilon_0 \chi_e E \tag{3.2}$$

3.2.1 Dielectric permittivity tensors

As mentioned earlier, ZrO_2 and HfO_2 are promising candidates to replace silicon-based dielectrics as dielectric gate material in modern integrated circuit technology due to their excellent dielectric properties and thermodynamic stability in contact with the Si substrate. However, the dielectric properties of the crystals are anisotropic and depend upon the lattice structures. So studying the dependence of the dielectric constant on the crystal phase and orientation is necessary for further application to select a suitable phase and its crystal orientation from the phases.

The static dielectric permittivity tensor ϵ^0_{ij} can be separated into two parts. first, the electronic contribution ϵ^∞_{ij} and ionic (lattice) contribution ion ϵ^{ion}_{ij}, the latter can be further decomposed in the contributions of different IR-active phonon modes m [67].

$$\epsilon^0_{ij} = \epsilon^\infty_{ij} + \epsilon^{ion}_{ij} = \epsilon^\infty_{ij} + \sum_m \Delta\epsilon_{m,ij} \tag{3.3}$$

where in 3.3 (i,j = 1,2,3 and m = 1,2,3...).

The dielectric permittivity tensors computed of both electronic contribution ϵ^∞_{ij} and ionic contribution ion ϵ^{ion}_{ij} are compared for monoclinic, ortho (Pca21), and tetragonal phases of HFO and ZRO. From the calculated values, it can be seen that firstly for all the phases of twin oxides, all-dielectric permittivity tensors of both electronic contribution ϵ_{ij}^{∞} and ionic contribution ϵ_{ij}^{ion} are symmetric about the leading diagonal, satisfying the symmetry of the crystal point-group.

To compare different phases of structures and between our current calculated values and previously available theoretical or experimental data, the approach to average the values of the leading diagonal elements are used because of the zero or negligible off-diagonal elements.

$$\epsilon^{\infty} = \frac{\epsilon_{11}^{\infty} + \epsilon_{22}^{\infty} + \epsilon_{33}^{\infty}}{3}$$

$$\epsilon^{ion} = \frac{\epsilon_{11}^{ion} + \epsilon_{22}^{ion} + \epsilon_{33}^{ion}}{3}$$

$$\epsilon^{\circ} = \epsilon^{ion} + \epsilon^{\infty}$$

Monoclinic

The monoclinic phase with the lowest point-group symmetry of 2/m as it can be seen from the figure among the other phases of HFO and ZRO. Thus having off-diagonal elements $\epsilon_{13}^{\infty} = \epsilon_{31}^{\infty} = 0.13$ and $\epsilon_{13}^{ion} = \epsilon_{31}^{ion} = 1.22$ for mono-HFO and $\epsilon_{13}^{\infty} = \epsilon_{31}^{\infty} = 0.14$ and $\epsilon_{13}^{ion} = \epsilon_{31}^{ion} = 1.46$ for mono-ZRO repectively. While it has been observed that for the other phases understudy, the dielectric permittivity tensors of both $\epsilon_{ij}^{\infty}$and ion ϵ_{ij}^{ion} are diagonal. Nevertheless, for all the phases of HFO and ZRO, the electronic contributions ϵ_{ij}^{∞} to the static dielectric constant are not too large enough, and neither strongly anisotropic nor strongly dependent on the structural phase. In contrast, the ionic contribution ion ϵ_{ij}^{ion} to the static dielectric constant is substantial, more anisotropic, and more sensitive to the structural phase. In the monoclinic phase, the low point-group symmetry of 2/m introduced the minor off-diagonal elementals to different leading diagonal elements.

The calculated dielectric tensor for mono-HFO is given as follow:

$$\epsilon^{ion}_{mono} = \begin{pmatrix} 15.2 & 0.00 & 1.22 \\ 0.00 & 13.5 & 0.00 \\ 0.122 & 0.00 & 10.8 \end{pmatrix}$$

$$\epsilon^{\infty}_{mono} = \begin{pmatrix} 4.84 & 0.00 & 0.13 \\ 0.00 & 4.85 & 0.00 \\ 0.13 & 0.00 & 4.58 \end{pmatrix}$$

The tensors from electronic contributions from other studies are 3.87 [60] and 3.32[68] for experiment and theoretical study, respectively. But the current reported average value (ϵ^{∞}) is 4.75, which is relatively high.

and for mono-ZRO is as:

$$\epsilon^{ion}_{mono} = \begin{pmatrix} 19.28 & 0.00 & 1.47 \\ 0.00 & 17.77 & 0.00 \\ 1.47 & 0.00 & 14.43 \end{pmatrix}$$

$$\epsilon^{\infty}_{mono} = \begin{pmatrix} 5.31 & 0.00 & 0.14 \\ 0.00 & 5.31 & 0.00 \\ 0.14 & 0.00 & 5.02 \end{pmatrix}$$

The dielectric tensors reported for mono-ZRO, especially ϵ^{ion}, are in good agreement with earlier reported values by Zhao *et al.* [69], and for ϵ^{∞}, the experimentally reported value is 4.8. However, in the present study, the average ϵ^{∞} (for electronic contribution) is 5.21, which is larger than the experimental one but comparable to other calculated reported values by DFT [67, 69, 70].

Tetragonal

The calculated dielectric tensors for tetragonal HFO are descibed below:

$$\epsilon^{ion}_{tetra} = \begin{pmatrix} 35.36 & 0.00 & 0.00 \\ 0.00 & 35.45 & 0.00 \\ 0.00 & 0.00 & 13.17 \end{pmatrix}$$

$$\epsilon^{\infty}_{tetra} = \begin{pmatrix} 5.15 & 0.00 & 0.00 \\ 0.00 & 5.15 & 0.00 \\ 0.00 & 0.00 & 4.64 \end{pmatrix}$$

The computed dielectric tensors for tetra-ZRO are such as:

$$\epsilon^{ion}_{tetra} = \begin{pmatrix} 43.67 & 0.00 & 0.00 \\ 0.00 & 43.67 & 0.00 \\ 0.00 & 0.00 & 13.16 \end{pmatrix}$$

$$\epsilon^{\infty}_{tetra} = \begin{pmatrix} 5.15 & 0.00 & 0.00 \\ 0.00 & 5.15 & 0.00 \\ 0.00 & 0.00 & 4.64 \end{pmatrix}$$

It has been reported that overall average dielectric values for tetragonal ZrO_2 and HfO_2 range from 34.5 [71] to 39.8 [72]. The values calculated from present calculations for the total dielectric constant of ZrO_2 and HfO_2 are 38.48 and 32.97, respectively.

Orthorhombic

The values dielectric tensors reported from earlier are 5.59 and 21.59 for ϵ^{∞} and ϵ^{ion} respectively [73]. But in current calculations the values are $\epsilon^{\infty} = 5.45$ and $\epsilon^{ion} = 23.99$ which are comparable to reported earlier. Dielectric tensors calculated for ortho-ZRO are such as:

$$\epsilon^{ion}_{ortho} = \begin{pmatrix} 27.36 & 0.00 & 0.00 \\ 0.00 & 24.45 & 0.00 \\ 0.00 & 0.00 & 20.17 \end{pmatrix}$$

$$\epsilon^{\infty}_{ortho} = \begin{pmatrix} 5.67 & 0.00 & 0.00 \\ 0.00 & 5.36 & 0.00 \\ 0.00 & 0.00 & 5.33 \end{pmatrix}$$

the calculated dielectric tensors for ortho-HFO are given below:

$$\epsilon^{ion}_{ortho} = \begin{pmatrix} 19.37 & 0.00 & 0.00 \\ 0.00 & 17.91 & 0.00 \\ 0.00 & 0.00 & 14.86 \end{pmatrix}$$

$$\epsilon^{\infty}_{ortho} = \begin{pmatrix} 5.10 & 0.00 & 0.00 \\ 0.00 & 4.89 & 0.00 \\ 0.00 & 0.00 & 4.85 \end{pmatrix}$$

The values dielectric tensors reported from earlier are 5.01 and 18.16 for ϵ^{∞} and ϵ^{ion} respectively [73]. But in current calculations the values are $\epsilon^{\infty} = 4.94$ and $\epsilon^{ion} = 17.38$ which are close to reported earlier.

Table 3.5: The average dielectric permittivity tensors of both electronic contribution ϵ^{∞} and ionic contribution ϵ^{ion} and total ϵ°

	Monoclinic			Orthorhombic			Tetragonal		
	($P2_1$/c)			($Pca2_1$)			($P4_2$/nmc)		
	ϵ^{∞}	ϵ^{ion}	ϵ°	ϵ^{∞}	ϵ^{ion}	ϵ°	ϵ^{∞}	ϵ^{ion}	ϵ°
HfO_2	4.75	13.16	17.91	4.94	17.38	22.32	4.98	27.99	32.97
ZrO_2	5.21	17.16	22.37	5.52	23.99	29.51	4.98	33.5	38.48

3.3 Born effective charge tensors

To evaluate the mixed covalent-ionic bonding in three phases of HFO and ZrO, the Born effective charge tensors (BEC, denoted by Z^*) are calculated by a linear response method concerning an external electric field.

The Born effective charge tensor governs the strength of Coulomb interaction responsible for the splitting between the longitudinal optical (LO) and transverse optical (TO) infrared-active phonon modes.

Born effective charge, also known as transverse or dynamic an effective charge is an essential quantity that manifests coupling between lattice displacements and electrostatic fields. Advances in ab-initio techniques now enable one to determine BEC theoretically using perturbation theory or finite difference in polarization. It has been found [74] that BEC values are relatively insensitive to isotropic volume change but are strongly affected by changes in atom positions associated with the phase transitions. BEC is vital in the theoretical study of ferroelectrics since the ferroelectric transition takes place from the competition of long-range Coulomb interactions and short-range forces. The Born effective charge tensor Z_{ij}^* is defined as a force ($\mathbf{F}_i$) in the direction i on one atom as a result of applying a unitary external electric field ($\mathbf{E}_i$) along the direction j

$$Z_{ij}^* = \frac{1}{e}\frac{\partial \mathbf{F}_i}{\partial \mathbf{E}_i} \qquad (i, j = 1, 2, 3) \tag{3.4}$$

The calculated Born effective charge tensors of the tetragonal, monoclinic, and orthorhombic phases of Hf_2 and Zr_2 are presented in Table 3.6, 3.6 3.8 respectively.

Firstly, it has been observed that for every atom, the Born effective charges are mainly distributed on the leading diagonal elements (Z_{ii}^*). Secondly, the magnitudes of $Z_{ii}^*(M)$ and $Z_{ii}^*(O)$ are more significant than their nominal ionic valences (+4 for Zr and Hf and -2 for O), indicating a robust dynamic charge transfer from M-atoms to oxygen atoms as the bond length changes and a composite covalent-ionic bonding in three different phases of MO_2. Due to their complex structures, the Born effective charge tensors are complicated in monoclinic and orthorhombic phases. For example, the non-equivalent two oxygen sites (O_I and O_{II}) and one cation lead to three kinds of atoms in the lattice. However, only one site symmetry leads to the Born effective charge tensors of all three kinds of atoms being neither diagonal nor symmetric.

Table 3.6: Born effective charge tensors Z^*_{ij} for tetragonal phase of ZrO_2 and HfO_2 (values in parentheses are other theoretical results for ZrO_2 [30] and HfO_2 [31] respectively.)

ZrO_2	Zr	O_I	O_{II}
xx	5.76 (5.75)	-3.74 (-3.50)	-3.74(-3.50)
yy	5.76 (5.76)	-2.02 (-2.34)	-2.02(-2.34)
zz	4.80 (5.37)	-2.40 (-2.59)	-2.40 (-2.59)
HfO_2	Hf	O_I	O_{II}
xx	5.49 (5.84)	-2.06 (-3.53)	-2.06 (-3.53)
yy	5.49 (5.84)	-3.43 (-2.50)	-3.43 (-2.50)
zz	4.75 (5.01)	-2.38 (-2.31)	-2.38 (-2.31)

Table 3.7: Born effective charge tensors $Z^{*}_{ij}$for monoclinic phase of ZrO_2 and HfO_2 (Values in parentheses are other theoretical results for ZrO_2[30] and HfO_2[31] respectively.)

ZrO_2	Zr		O_{I}		O_{II}	
xx	5.48	(5.45)	-3.02	(-3.02)	-2.45	(-2.46)
xy	-0.35	(-0.43)	1.19	(1.17)	0.21	(0.17)
xz	0.20	(0.18)	-0.19	(-0.19)	-0.01	(0.02)
yx	-0.21	(-0.16)	1.43	(1.45)	0.25	(0.24)
yy	5.42	(5.61)	-2.69	(-2.76)	-2.73	(-2.86)
yz	-0.23	(-0.15)	-0.67	(-0.69)	0.35	(0.37)
zx	0.20	(0.12)	-0.18	(-0.19)	-0.03	(-0.02)
zy	0.36	(0.38)	-0.74	(-0.68)	0.35	(0.41)
zz	4.97	(4.97)	-2.36	(-2.23)	-2.62	(-2.66)
HfO_2	Hf		O_{I}		O_{II}	
xx	5.29	(5.57)	-2.91	(-3.10)	-2.37	(-2.47)
xy	-0.35	(-0.56)	1.05	(0.90)	0.15	(0.15)
xz	0.21	(0.91)	-0.21	(-0.53)	0.01	(-0.36)
yx	-0.16	(-0.02)	1.26	(1.29)	0.21	(0.11)
yy	5.25	(5.57)	-2.56	(-2.79)	-2.69	(-2.87)
yz	0.17	(0.07)	-0.65	(-0.61)	0.34	(0.40)
zx	0.22	(0.27)	-0.18	(-0.20)	-0.03	(-0.09)
zy	0.33	(0.45)	-0.67	(-0.51)	-0.40	(0.46)
zz	4.79	(4.64)	-2.26	(-2.16)	-2.53	(-2.52)

Table 3.8: Born effective charge tensors Z^*_{ij} for orthorhombic phase of ZrO_2 and HfO_2 (values in parentheses are other theoretical results for ZrO_2 [30].)

ZrO_2	Zr		O_I		O_{II}	
xx	5.74	(5.45)	-3.07	(-3.02)	-2.64	(-2.46)
xy	-0.17	(-0.43)	0.78	(1.17)	-0.32	(0.17)
xz	0.39	(0.18)	0.80	(-0.19)	-0.10	(0.02)
yx	-0.28	(-0.16)	0.77	(1.45)	-0.24	(0.24)
yy	5.19	(5.61)	-2.59	(-2.76)	-2.59	(-2.86)
yz	-0.06	(-0.15)	0.33	(-0.69)	-0.28	(0.37)
zx	-0.03	(0.12)	1.05	(-0.19)	-0.14	(-0.02)
zy	0.02	(0.38)	0.31	(-0.68)	-0.24	(0.41)
zz	5.28	(4.97)	-2.56	(-2.23)	-2.71	(-2.66)
HfO_2	Hf		O_I		O_{II}	
xx	5.29		-2.91		-2.37	
xy	-0.35		1.05		0.15	
xz	0.21		-0.21		0.01	
yx	-0.16		1.26		0.21	
yy	5.25		-2.56		-2.69	
yz	0.17		-0.65		0.34	
zx	0.22		-0.18		-0.03	
zy	0.33		-0.67		-0.40	
zz	4.79		-2.26		-2.53	

3.4 Ferroelectricity

The non-centrosymmetric crystals possess a unique axis of symmetry. These crystals are named polar. Piezoelectric rics that are polar crystals also exhibit pyroelectric. Then when their temperature is changed, charges will appear on their surfaces. Polar structures have a dielectric polarization built into the unit cell of the crystal structure. This is regarded as spontaneous polarization. The application of stress or a change in temperature causes a change in this dipole moment, which causes the separation of charge on the surfaces of the crystal. The direction and magnitude of the spontaneous polarization in a polar dielectric can be changed by applying an electric field. Still, on removing the field, it will return to its zero-field value. The spontaneous polarization is calculated for three different phases for both bulk HfO_2 and ZrO_2. Ferroelectricity is, in many cases associated with a structural phase transition from a higher symmetric to a lower polar phase symmetric polar. The ferroelectricity in HfO_2 and ZrO_2 arises from the polar (non-centrosymmetric) orthorhombic phases. HfO_2 and ZrO_2 undergo structural phase transitions. These are monoclinic, tetragonal, and cubic, which appear by the successive phase transitions, and have been well studied. Some of them have an inversion center that does not show ferroelectricity [75].

As the atoms deviate from their centrosymmetric positions in the unit cell, it affects the bond lengths between cation and anion, resulting in more distortions and polarization in either direction. Because it is found that structural relaxation has a significant effect on the chemical bonding, which later causes a remarkable impact on the polarization [76].

To quantitatively illustrate, the spontaneous polarization (P_s) where, $s = x, y, z$ is calculated in each case as [76]:

$$P_s = \frac{e}{V} \sum_{i}^{N} Z_n^* \delta_{z_i} \tag{3.5}$$

Where e is the electronic charge (1.6×10^{-19} C), V is the total volume of the unit cell, Z_n^* is the Born effective charge for n-th atom, and δ_{z_i} is the relative displacement between the ith cation and O anion in the respective plane. The spontaneous polarization for each phase is computed using flexible axes structure. Consequently, the relaxation results in decreased atomic layer distance between the first and second top cation layers compared to unrelaxed ones.

The value of calculated polarization using the eqs. 3.5 and using calculated born effective charges are for ZrO_2 and HfO_2 are given in Table. 3.10 and 3.9.

Table 3.9: Computed P_s $(s = x, y, z)$ in μCcm^{-2} for three phases ZrO_2.

Phases	space group	PBE	PBE+U	mBj	mBJ+U
Mono	$P2_1/c$	$P_x = 0.03$	0.06	0.03	0.06
		$P_y = 0.05$	0.06	0.05	0.06
		$P_z = 1.74$	2.01	1.74	2.02
Ortho	$Pca2_1$	$P_x = 9.63$	9.48	9.62	9.34
		$P_y = 12.42$	12.01	12.40	12.05
		$P_z = 32.45$	33.01	32.45	33.01
Tetra	$P4_2/nmc$	$P_x = 0.01$	0.01	0.00	0.01
		$P_y = 0.02$	0.04	0.03	0.04
		$P_z = 6.00$	6.05	5.98	6.05

Table 3.10: Computed P_s $(s = x, y, z)$ in μCcm^{-2} for three phases HFO_2.

Phases	space group	PBE	PBE+U	mBj	mBJ+U
Mono	$P2_1/c$	$P_x = 0.06$	0.07	0.06	0.07
		$P_y = 0.08$	1.00	0.08	1.01
		$P_z = 1.74$	2.01	1.74	2.02
Ortho	$Pca2_1$	$P_x = 5.08$	6.21	5.08	6.21
		$P_y = 16.73$	17.01	16.73	17.02
		$P_z = 38.45$	39.27	38.45	39.25
Tetra	$P4_2/nmc$	$P_x = 0.08$	0.08	0.08	0.08
		$P_y = 1.07$	2.00	1.07	2.00
		$P_z = 10.23$	11.43	10.23	11.44

In comparison with other reported theoretical results from [75][30] the present values for both oxides are overestimated. A significant amount of spontaneous polarization has been detected in the orthorhombic phase of both oxides. The four Hf/Zr atoms form a distorted crystal structure, with the eight O atoms occupying the pseudo-tetrahedral interstitial site. The $Pca2_1$ and P/mnc phases reveal that oxygen atoms shift along with the c-axis, allowing spontaneous polarization.

The above results show that HfO_2 has a slightly higher polarization value than ZrO_2. For monoclinic phase the c/a ratio is 1.037 and 1.023 for HfO_2 and ZrO_2, repectively. For orthorhombic phase the c/a ratio is 1.042 and 1.062 for HfO_2 and ZrO_2, repectively. The HfO_2 structure is more distorted as compared to ZrO_2 which can be a reason of higher value of polarization. Also, for tetragonal phase ZrO_2 has less c/a ratio as compared to HfO_2. To check the effect of Hubbard potential (U) on spontaneous polarization. It has been discovered that compared to calculations performed with PBE, the atomic positions were changed slight. The difference between spontaneous polarization using PBE and PBE+U is in the order of 0.01-0.04, 0.023, and 0.12 for monoclinic, tetragonal, and orthorhombic phases, respectively for HfO_2.

3.5 Electronic Properties

The density of states (DOS) is another important property that plays a significant role in analyzing electronic properties. The DOS at a specific energy level signifies the number of vacant states available for an electron to occupy. The contribution of different atoms can be illustrated from total and partial DOS plots. The bandgap (The term "bandgap" refers to the energy difference between the top of the valence band and the bottom of the conduction band. When the electronic band structure is described graphically, the valence band lies below the Fermi level and the conduction band above the Fermi level. The top of the valence band is called valence band maximum (VBM), and the bottom of the conduction band is referred to as (CBM). So, the electrons can jump from one band to another by absorbing or releasing an amount of energy equal to the bandgap. It usually happens in semiconductors and is crucial in forming necessary devices for semiconductor applications. In the present work, the valence band maximum energy (E_{VBM}) is set as zero.

3.5.1 Band gap for HfO_2 and ZrO_2

Table 3.11: Computed band gap energies (E_g) in eV from the structures under investigation.

Phases	PBE	PBE+U	mBJ	mBJ+U	Theo.	Exp.
m-HfO_2	4.02	4.27	6.10	6.40	3.36[60],5.79[59]	5.80^{Ni}
m-ZrO_2	3.64	3.86	4.59	4.99	3.60[77], 5.80[77]	5.80[78]
o-HfO_2	4.35	4.63	6.43	6.57	4.75[31]	5.67[79]
o-ZrO_2	3.83	4.09	4.80	5.23	4.46[79]	4.70[79] 5.90[80]
t-HfO_2	4.66	4.72	6.61	6.67	4.36[81], 5.78[81]	5.86 [82]
t-ZrO_2	4.02	4.23	4.97	5.47	4.11[81]	5.90[83]

Monoclinic

Fig. 3.4(a) and (b) and 3.5(a) and (b) represents the total DOS curves for monoclinic HfO_2 and ZrO_2, The TDOS is represented between the energy range -6eV to 10 eV. In the general analysis for PBE calculated DOS, it has been analyzed that both hafnia and zirconia are composed of three prominent bands: the lower valence band ranges between -16.13 and -15.5 eV, the valence band just below the Fermi level lies in between -6.8 and 0 eV. The lower valence band is composed of mainly O 2s orbitals. O 2p states control the valence band near the VBM (as shown in Fig. 3.4(e) and (f)) and3.6, with a minor presence of Hf/Zr-5d states (Fig. 3.4 and 3.6(c) and (d)). The

presence of Hf/Zr 4p and 4s states in the valence band range is small. From Fig 3.4 and 3.6(c)(d), it can be seen that the unoccupied conduction band consists essentially of Hf/Zr 5d/4d states, separated from the valence band by an energy gap of 4.022 eV and 3.64 eV for HfO_2 and ZrO_2, respectively.
To improve the bandgap, the approach to induce Hubbard potential (U) considered to produce improve the bandgap, the $U^d = 3$ eV for 5d orbitals on the Hf atom is introduced. As illustrated in Fig. 3.4 and 3.6 when $U^d =$ 3 eV is applied on cation on d-orbital. The application of U^d decreases the width of the valence band by 0.1 eV. In contrast, the conduction band mainly comprises d-states that shift towards higher energy levels by 0.25 eV and 0.22 eV for HfO_2 and ZrO_2, respectively. This overall results in an increase in the bandgap.
Since standard semi-local GGA underestimates band gap [38, 84], the exchange and correlation effect is also treated using the mBJ [85]. Subsequently, mBJ and mBJ+U are employed with $U^d = 3$ eV for d orbitals on the cations. The total DOS (TDOS) along with partial DOS (PDOS) for mBJ and mBJ+U are shown in Fig. 3.5 and 3.7 for HfO_2 and ZrO_2, respectively. It has been observed that while using mBJ-potential, the bottom of the valence band has been shifted towards the E_{VBM} or lower energy levels, while the shift in the conduction band towards higher energy levels have also been observed. These shifts yield a wider band gap for both HfO_2 and ZrO_2. For example, the band gap value obtained for monoclinic HfO_2 using mBJ is 6.10 eV which is in excellent agreement with other theoretically values using mBJ which is 6.08 eV. The present mBJ value (6.10 eV) for HfO_2 is in excellent agreement with the theoretical value of 6.08 eV using mBJ [86].

The band gaps estimated during the present calculations are presented in the Table 3.11.

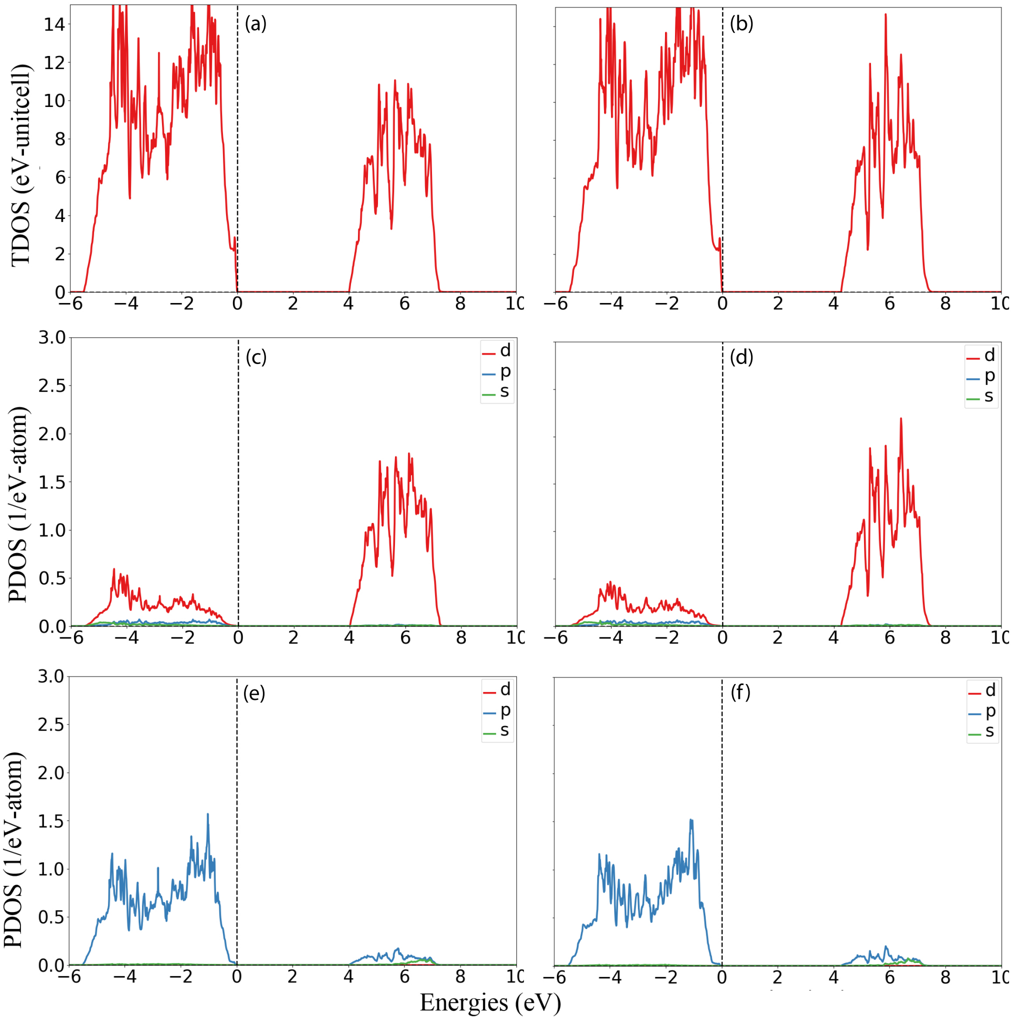

Figure 3.4: Total DOS for monoclinic HfO_2 (a) PBE (b) PBE+U. Partial DOS for (c) Hf and (e) O for PBE and (d) Hf (f) O for PBE+U. The dotted line at zero energies represents the VBM and E_{VBM} are set at zero.

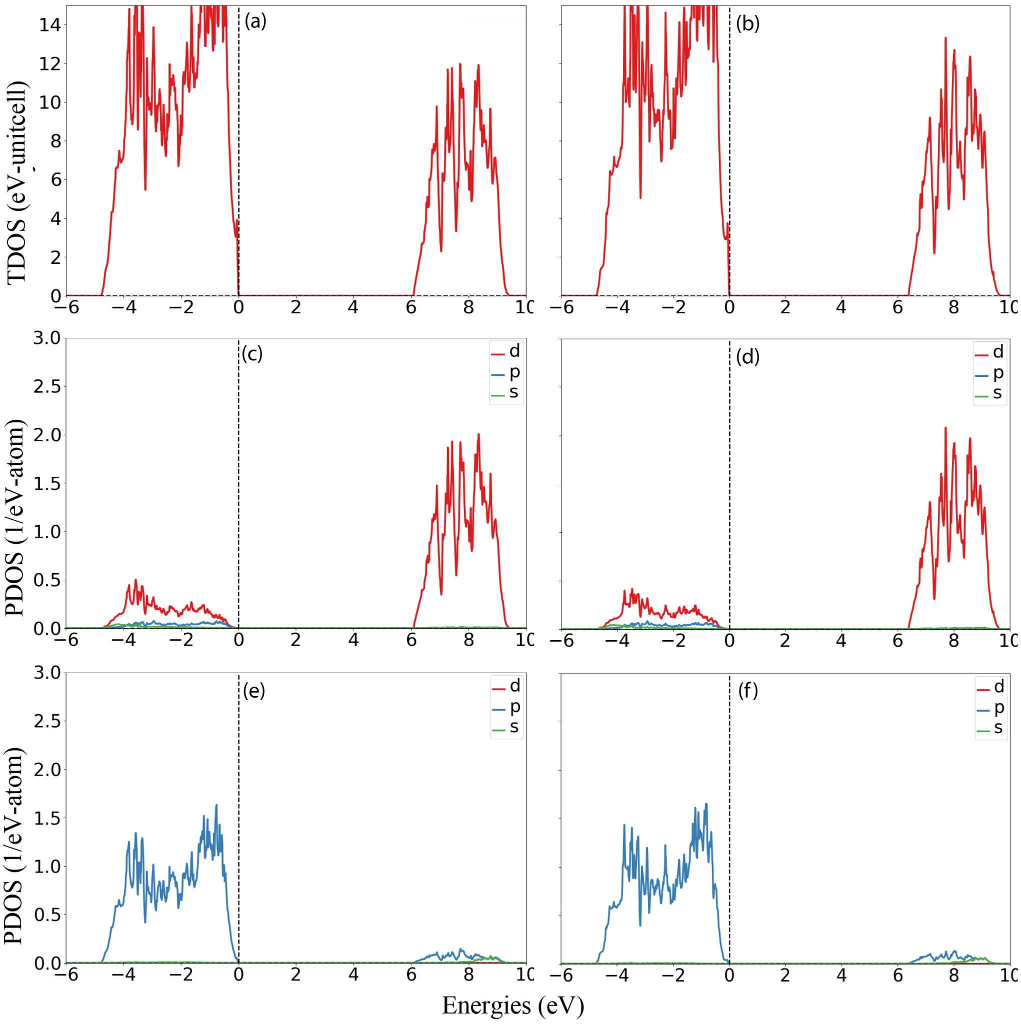

Figure 3.5: Total DOS for monoclinic HfO_2 (a) mBJ (b) mBJ+U. Partial DOS for (c) Hf and (e) O for mBJ and (d) Hf (f) O for mBJ+U.

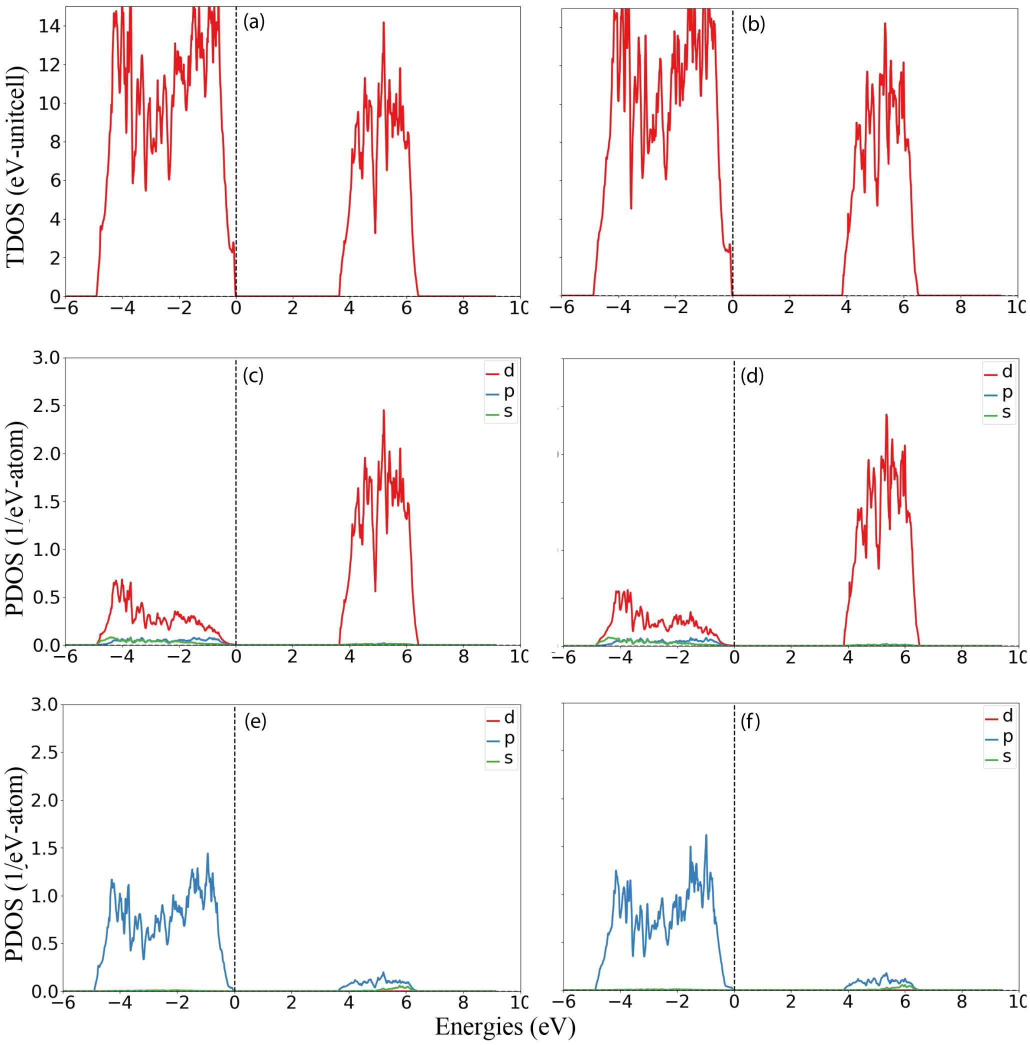

Figure 3.6: Total DOS for monoclinic ZrO_2 (a) PBE (b) PBE+U. Partial DOS for (c) Hf and (e) O for PBE and (d) Hf (f) O for PBE+U.

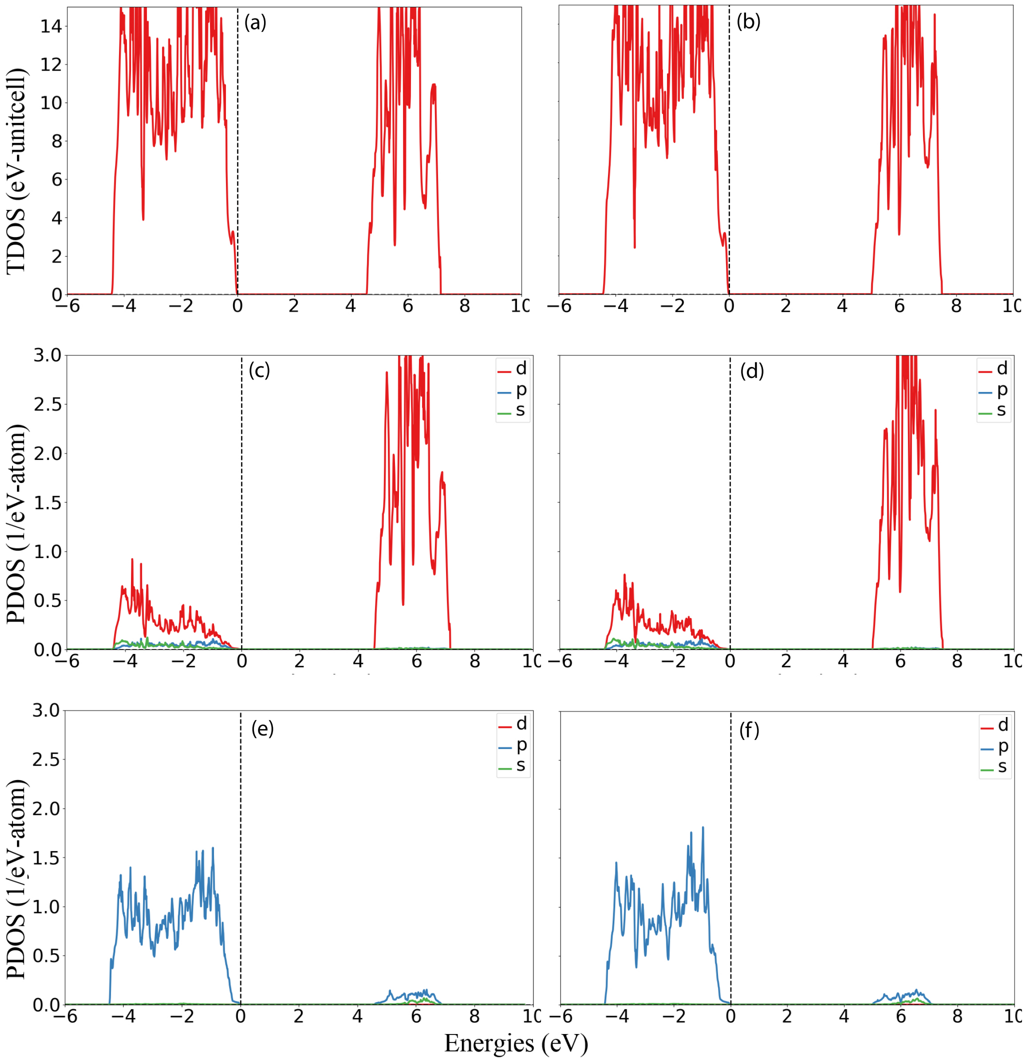

Figure 3.7: Total DOS for monoclinic ZrO_2 (a) mBJ (b) mBJ+U. Partial DOS for (c) Hf and (e) O for mBJ and (d) Hf (f) O for mBJ+U.

Tetragonal

For tetragonal phase of HfO_2 and ZrO_2, TDOS and PDOS are represented in Fig. 3.8 and 3.9 for energy range -6 eV to 10 eV. The lower valence band lies between -18.3 eV to -16 eV mainly composed of O 2s and Hf/Zr 5d/4d orbitals. While below the E_{VBM} (between -5.7 eV to 0 eV) lies upper valence band. The main contribution towards the upper valence band comes from O 2p (see Fig 3.8 and 3.9(e)(f) in blue lines, with little contribution from

Hf-5d/Zr-4d as depicted in fig 3.8 and 3.8 (c)(d) for both PBE and PBE+U. When $U^d = 3$ eV is applied of Hf-5d/Zr-4d the bandgap is increased by almost 0.2 eV for HfO_2 and 0.1 eV for ZrO_2. The largest band gap of all hafnia/zirconia polymorphs is predicted for the tetragonal structure while utilizing PBE and mBJ and even with application of U^d. The band gap predicted using mBJ (6.61 eV) for HfO_2 is more close to experimental value (5.86 eV [82]) while mBJ+U predicts it be 0.6 eV larger as comapared to experimental. Meanwhile, for ZrO_2 band gap predicted using mBJ+U (5.47 eV) is close to experimental value of 5.90 ev [83].

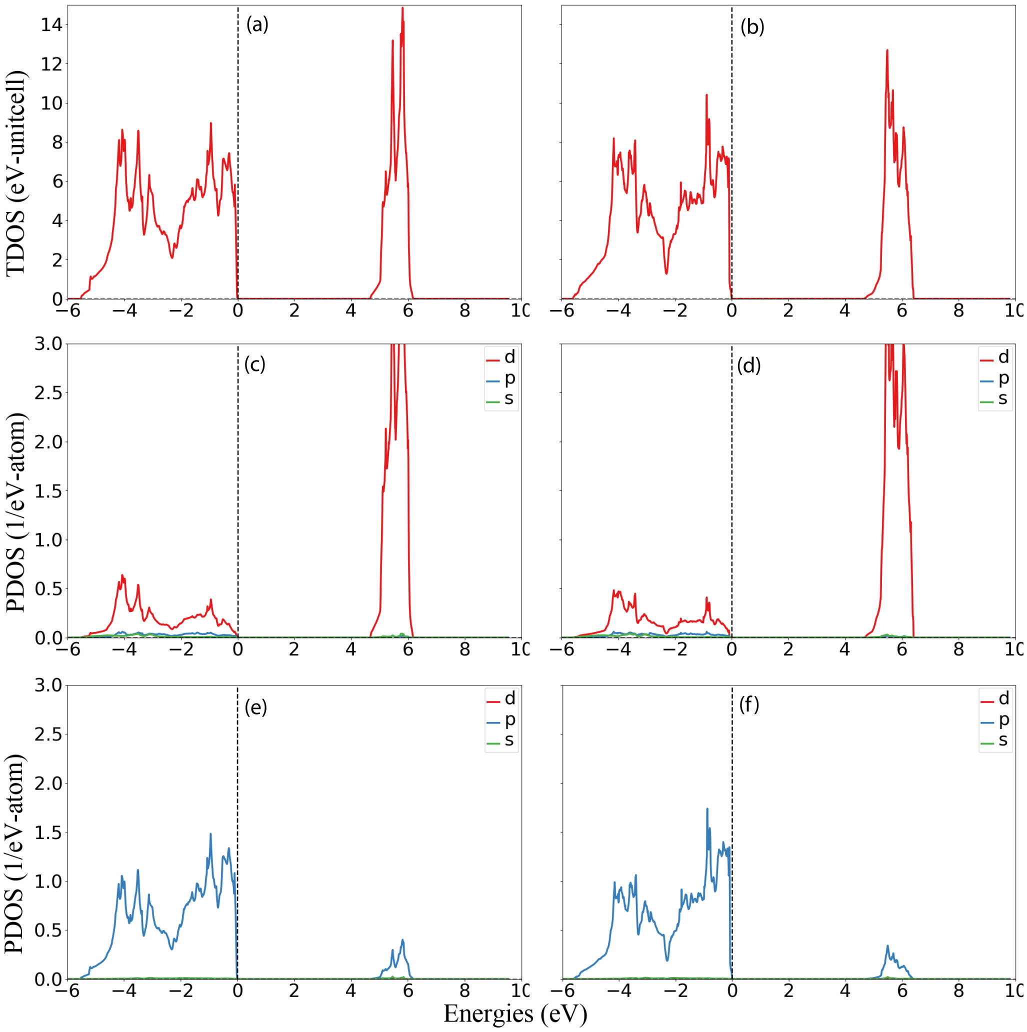

Figure 3.8: Total DOS for tetragonal HfO_2 (a) PBE (b) PBE+U. Partial DOS for (c) Hf and (e) O for PBE and (d) Hf (f) O for PBE+U.

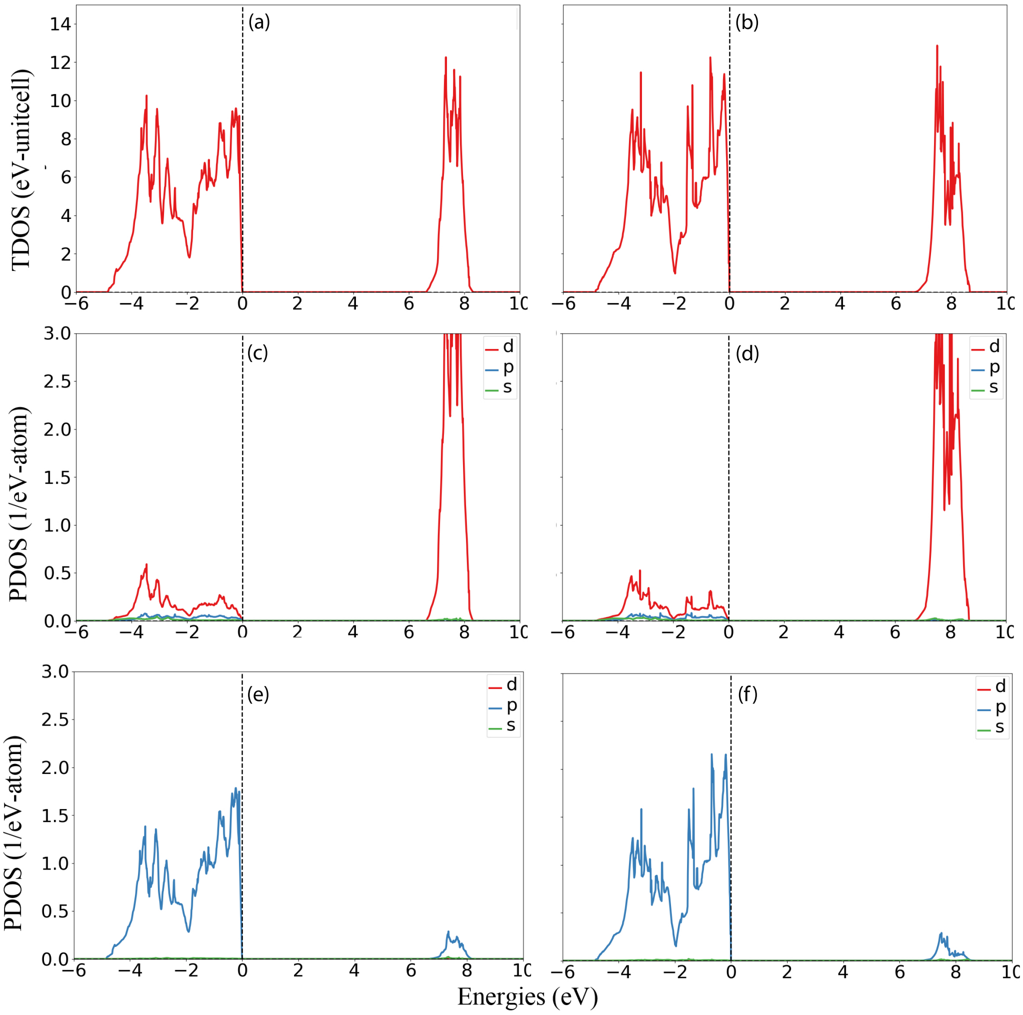

Figure 3.9: Total DOS for tetragonal HfO_2 (a) mBJ (b) mBJ+U. Partial DOS for (c) Hf and (e) O for mBJ and (d) Hf (f) O for mBJ+U.

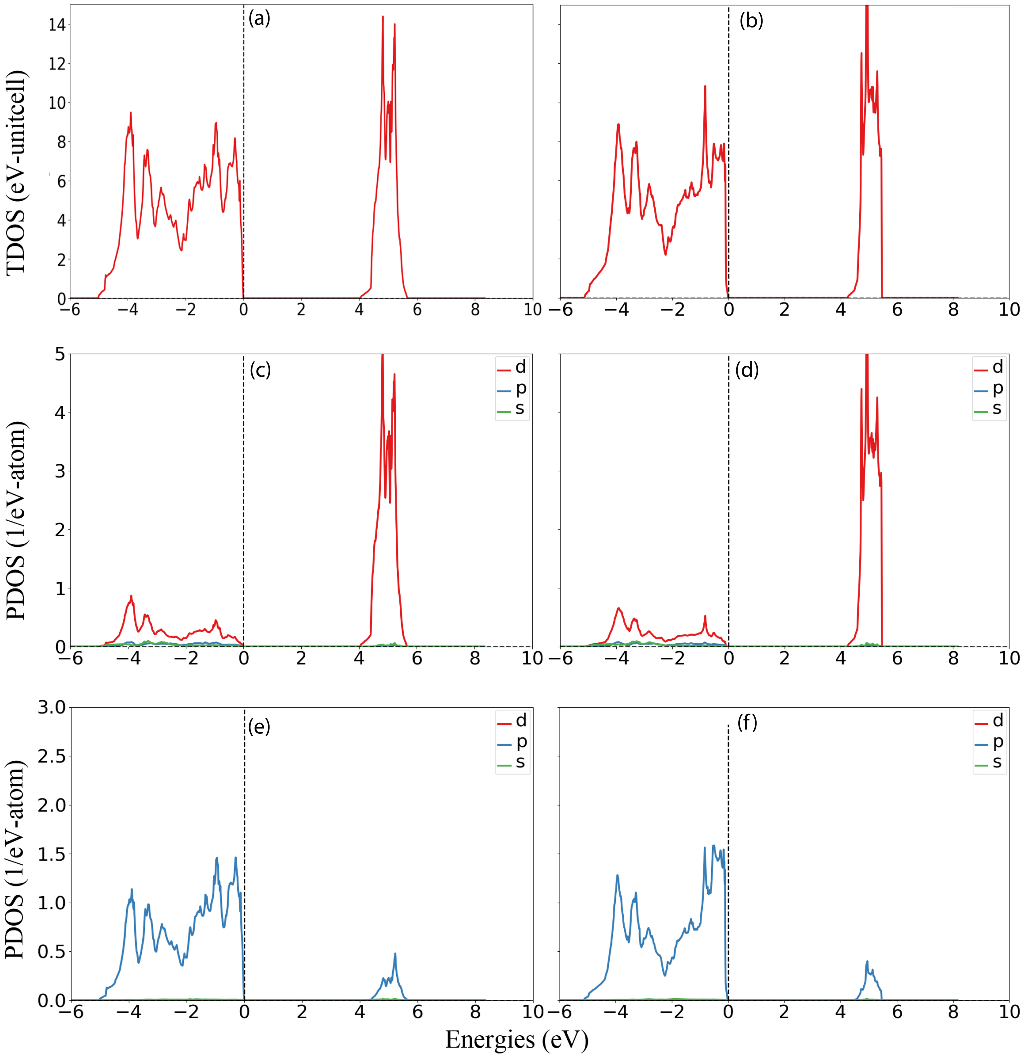

Figure 3.10: Total DOS for tetragonal ZrO_2 (a) PBE (b) PBE+U. Partial DOS for (c) Hf and (e) O for PBE and (d) Hf (f) O for PBE+U.

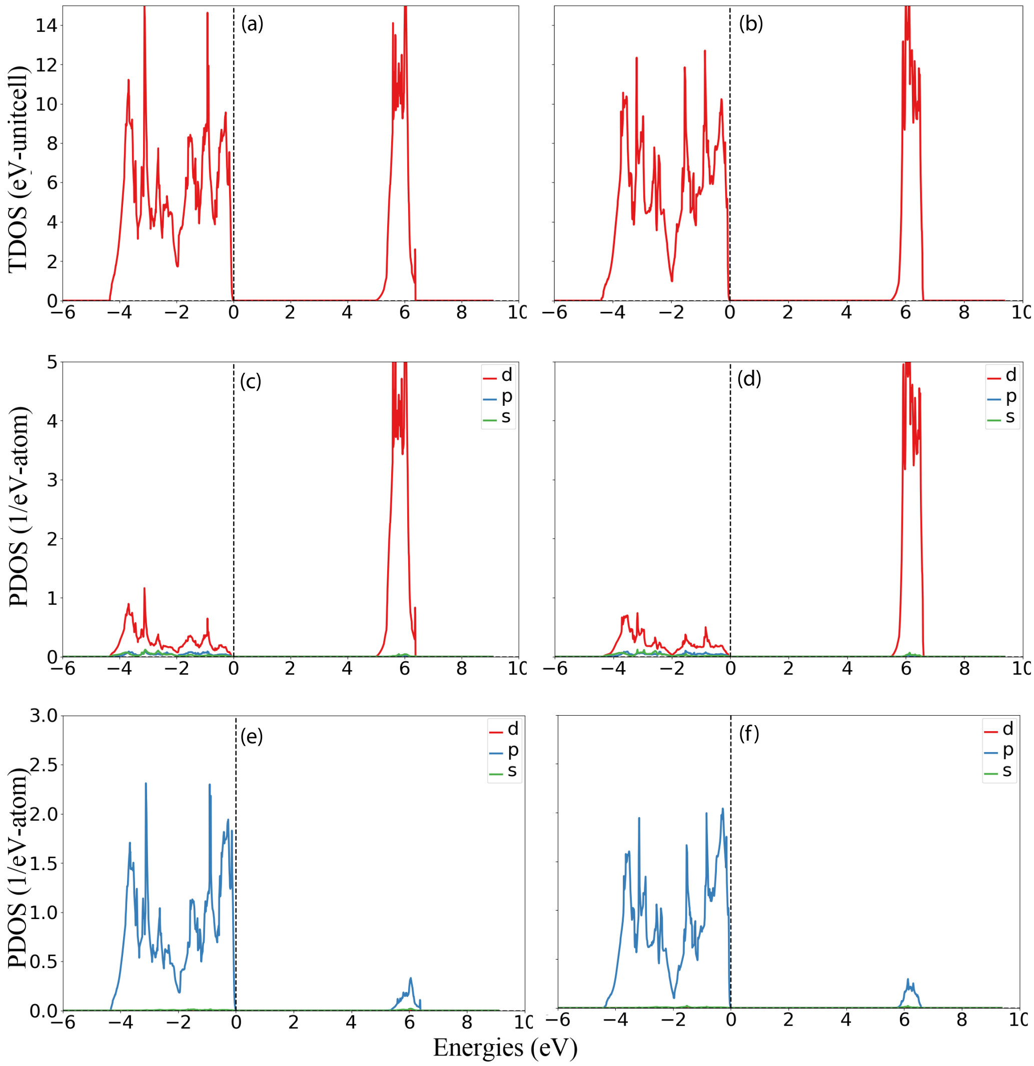

Figure 3.11: Total DOS for tetragonal ZrO_2 (a) mBJ (b) mBJ+U. Partial DOS for (c) Hf and (e) O for mBJ and (d) Hf (f) O for mBJ+U.

Orthorhombic

For orthorhombic phase of Hf_2 and Zr_2 TDOS per unit cell are shown in Fig. 3.12 and 3.14. As described in previously studied structures, the lower valence band is mainly dominated by 2p orbitals of O, as illustrated in Fig. 3.12 and 3.14(e)(f), overlaps with a minor contribution from 6s, 5p, and 5d orbitals of Hf/Zr. Where 5d/4d orbitals of Hf/Zr mainly contribute to the conduction band, and O has less contribution to the conduction band. The insertion of U^d on d orbital of cation is responsible for the shift in states, mainly d states and results in increase in the energy gap between VBM and CBM by 0.28 eV and 0.26 eV for HfO_2 and ZrO_2, respectively.

Fig. 3.13 and 3.15 depicts the TDOS per unit cell alongside PDOS per atom of cation and O. As described earlier for former structures, the band gap modifies with mBJ. The same trend is observed for the orthorhombic phase also. For example, for HfO_2, the mBJ potential predicts the band gap to be 0.38-0.76 eV, more considerable than the experimental 5.67 eV [79]. Contrary to that, for the orthorhombic phase of ZrO_2, both mBJ (4.80 eV) and mBJ+U (5.23 eV) predicted band gaps are close to band gaps of 4.70 eV [79] and 5.90 eV experimentally [80].

Finally, all mBJ calculated band gaps are significantly increased and improved towards experimental values compared with the PBE values for most polymorphs. Overall, for all phases of both oxides the valence band (VB) of -0.5 to 0 eV is mainly constructed from the O 2p states, which hybridized strongly with Zr 4d and Hf 5d states, indicating stronger covalent bonding. The unoccupied band is contributed chiefly by cation d-states followed by O 2p states. It is well known that traditional DFT functionals such as PBE underestimates the energy band gap in insulators because these functionals are not accurate in describing systems with localized strongly correlated d and f electrons. This lack of accuracy of the DFT functionals has been solved by introducing a solid intra-atomic interaction, known as on-site coulomb interaction. The U correction was applied both to the d states of cations. The implication of U is aimed to improve localization of d and f-states. In the energies below VB there are strong O-p states. By comparing PBE with PBE+U and also for mBJ and mBJ+U, there is an increase in the band gap value due to the U correction and a "sharpening" of the PDOS due to the higher level of localization of states that are corrected.

Comparing estimated band gaps with PBE and mBJ, it has been analyzed that the main change in mBJ calculations is in the position of unoccupied states in conduction band (CB). So, the mBJ potential narrows the Hf 5d and Zr 4d band and shifts it towards higher energies, increasing the band gap w.r.t PBE calculations. the width of VB using mBJ is reduced by 0.5 eV and 0.7 eV for HfO_2 and ZrO_2, respectively. Hence, the discrepancy between the experimental and theoretical band gaps is significantly reduced with semi-local exchange and correlation effects. As a result, the band gap values computed using them for solids have a good agreement with experimental data.

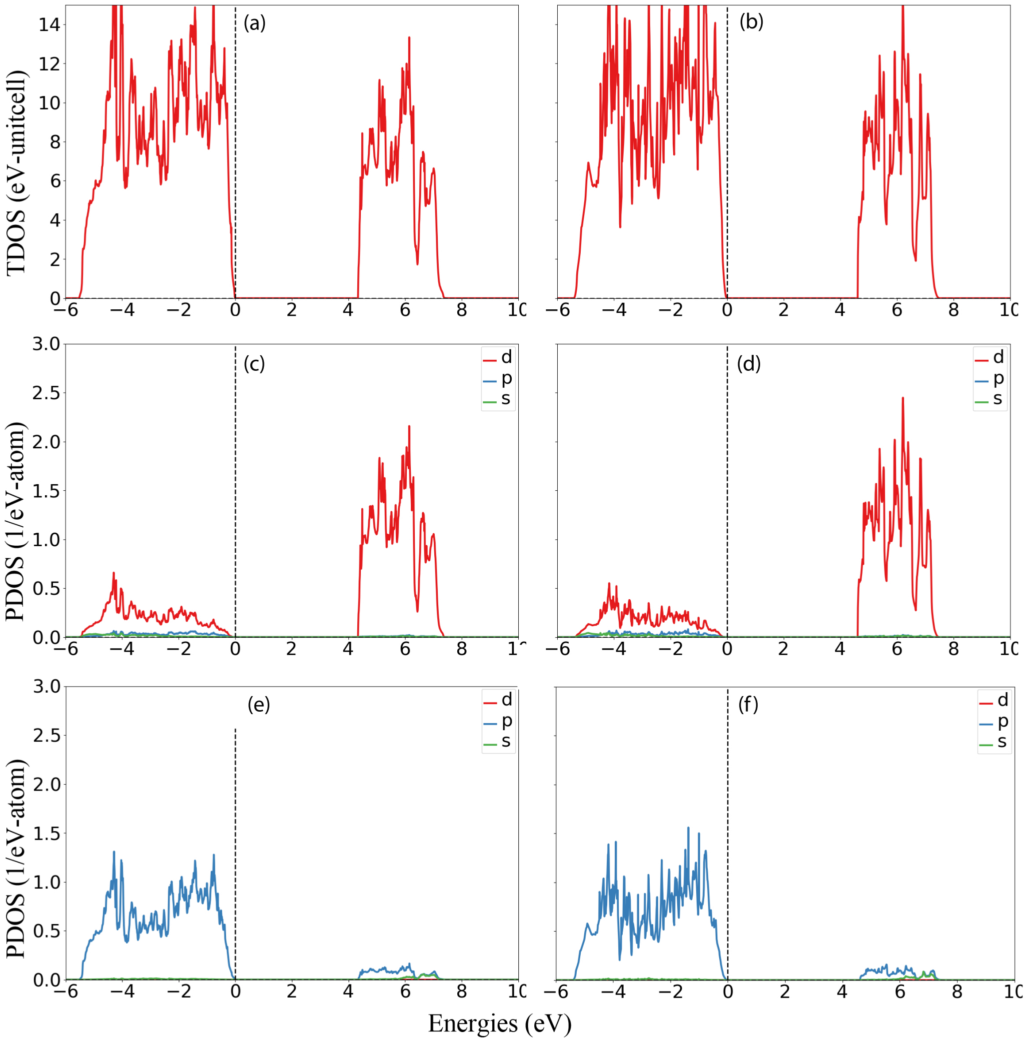

Figure 3.12: Total DOS for orthorhombic HfO_2 (a) PBE (b) PBE+U. Partial DOS for (c) Hf and (e) O for PBE and (d) Hf (f) O for PBE+U.

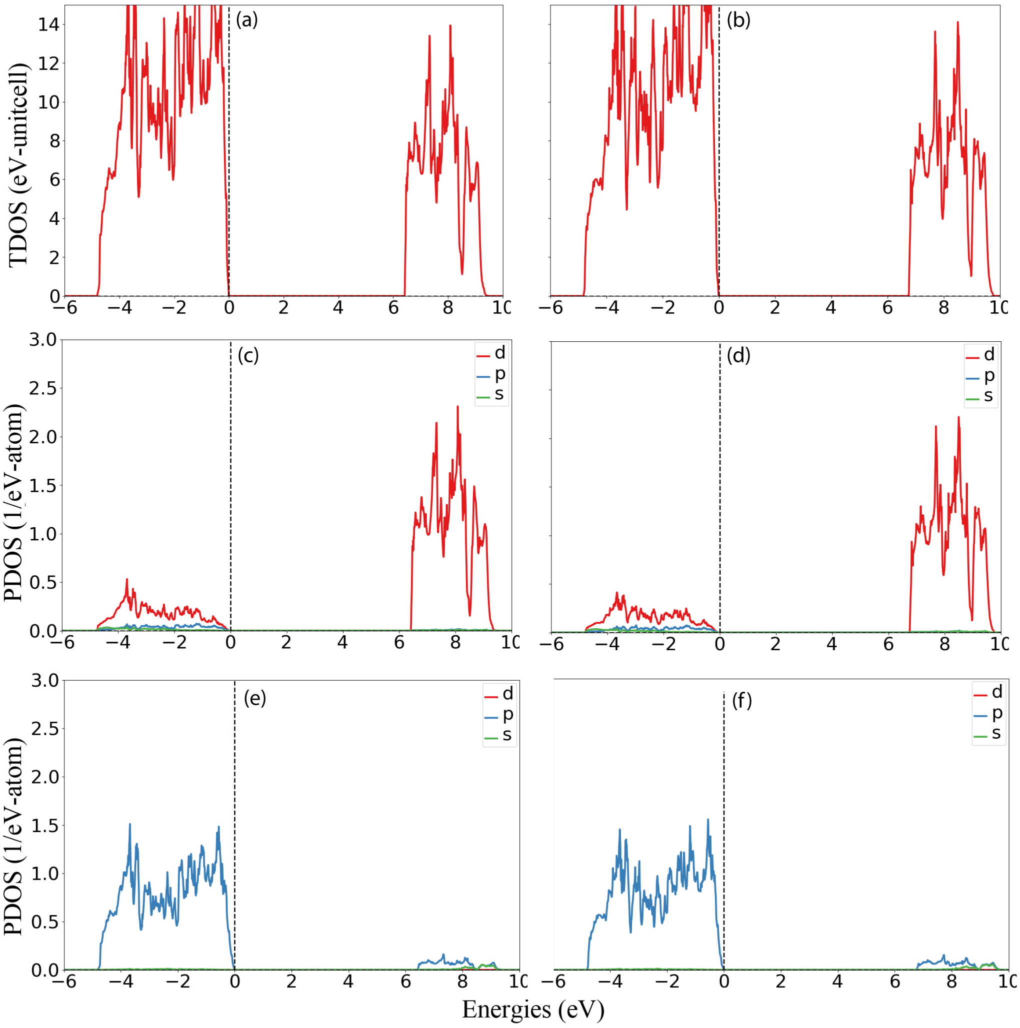

Figure 3.13: Total DOS for orthorhombic HfO_2 (a) mBJ (b) mBJ+U. Partial DOS for (c) Hf and (e) O for mBJ and (d) Hf (f) O for mBJ+U.

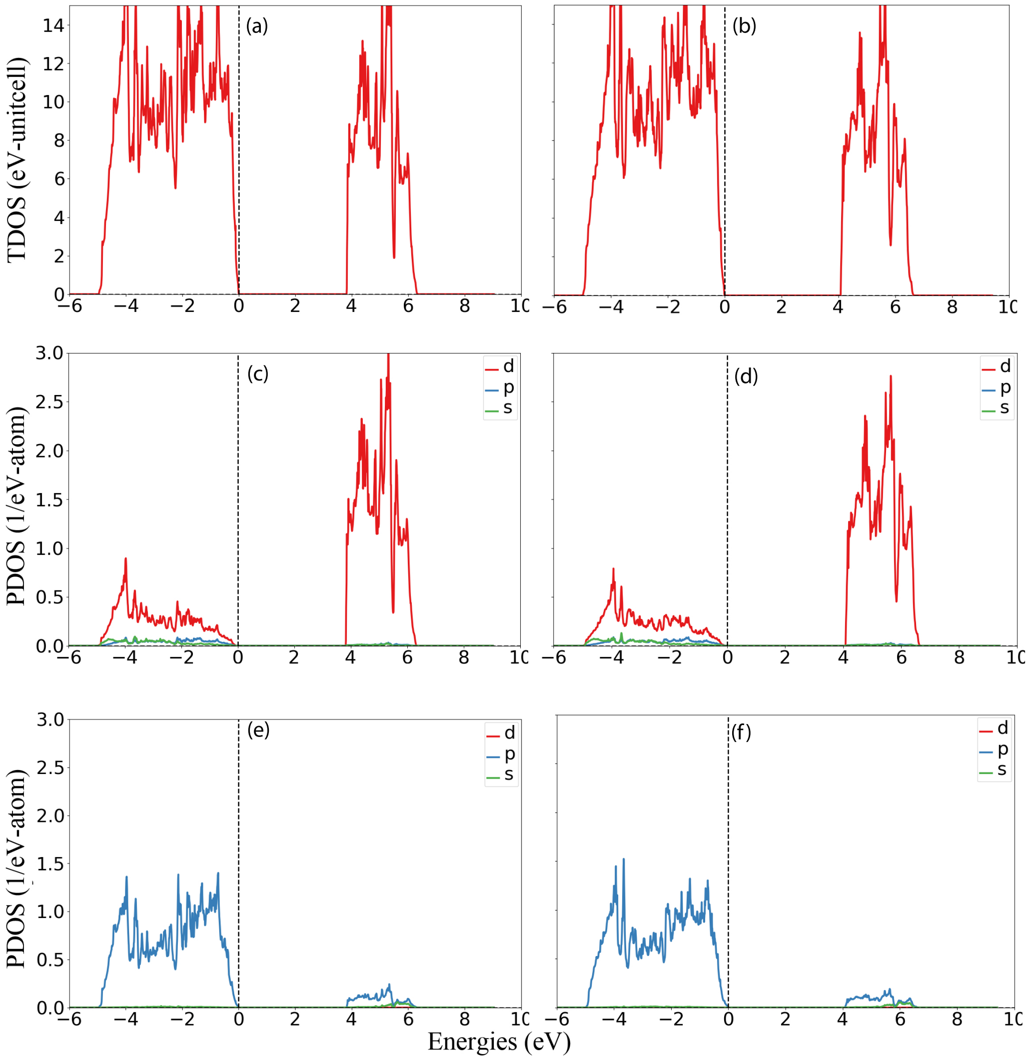

Figure 3.14: Total DOS for orthorhombic ZrO_2 (a) PBE (b) PBE+U. Partial DOS for (c) Hf and (e) O for PBE and (d) Hf (f) O for PBE+U.

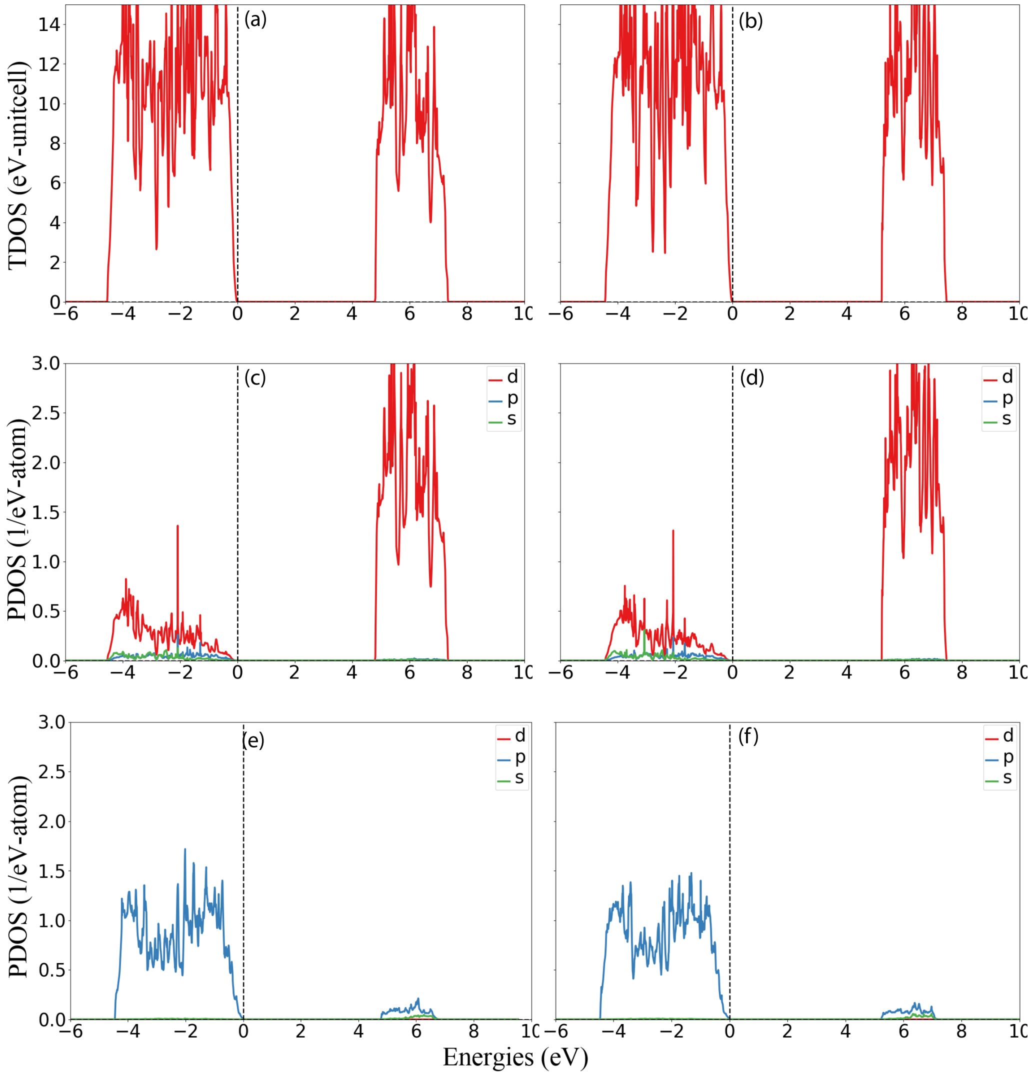

Figure 3.15: Total DOS for orthorhombic ZrO_2 (a) mBJ (b) mBJ+U. Partial DOS for (c) Hf and (e) O for mBJ and (d) Hf (f) O for mBJ+U.

3.5.2 Ferroelectric and electronic properties of periodic layered Structures of HfO_2 and ZrO_2

HfO_2/ZrO_2 based ferroelectric memory devices have been the focus of research due to their promising results regarding non-remanent polarization [87]. Especially for ferroelectric tunnel junctions based on HfO_2/ZrO_2 layered or hetrostructures can overcome some limitations from ferroelectric memories, e.g., by having a nondestructive read-out [88]. Accordingly, the supercell of 1 × 1 × 6 for HfO_2 is constructed for the orthorhombic and tetragonal phase with single and two-layer of Zr at cation site. The big supercell in the z-direction is constructed instead of the smaller one to observe the layered effect more accurately; that might not be possible for a small structure. Such as, $(HfO_2)_n/(ZrO_2)_n$, n is the number of layers for HfO_2 and ZrO_2, respectively. In the present study, the 50 % mix of Hf with Zr atoms is chosen, thus n for HfO_2 is equal to ZrO_2.

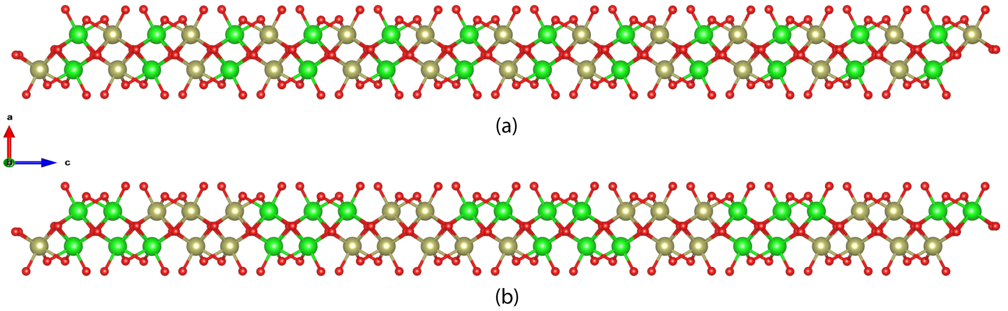

Figure 3.16: Structural representation of (a) $(HfO_2)_1/(ZrO_2)_1$ (b) $(HfO_2)_2/(ZrO_2)_2$. The green balls represents Zr atoms while yellow and red represents Hf and oxygen atoms, respectively.

orthorhombic

The orthorhombic phase is found to have the highest value of polarization among other phases studied. The crystal structure representation of $(HfO_2)_n/(ZrO_2)_n$ structures is in Fig. 3.16. The polarization is calculated using eqs. 3.5 as single layer and two layer of Zr content in super-cell. Like the primitive structures the polarization is found to be prominent in z-direction that is $P_z = 41.64\ \mu\text{Ccm}^{-2}$ and $P_z = 44.37\ \mu\text{Ccm}^{-2}$ for $(HfO_2)_1/(ZrO_2)_1$ and $(HfO_2)_2/(ZrO_2)_2$, respectively. The other directions also found to have almost some value for spontaneous polarization that is almost $P_x = 3.34$ μCcm^{-2} and $P_y = 7.23\ \mu\text{Ccm}^{-2}$. From the other studies it has been found that $(HfO_2)/(ZrO_2)$ based thin film show remnant polarization about 12μ

Ccm^{-2} for thickness of 12 nm [89]. The estimated band gaps for layered structures along with spontaneous polarization is depicted in 3.12.

Table 3.12: Computed band gap energies (E_g) in eV and spontaneous polarization P_x, P_y and P_z in μCcm^{-2} for $(HfO_2)_n/(ZrO_2)_n$, n = 1, 2 in orthorhombic phase.

	PBE	PBE+U	mBJ	mBJ+U
n = 1				
	4.09	4.26	5.06	5.77
P_x	3.34	3.94	3.34	3.91
P_y	7.23	8.01	7.20	8.03
P_z	41.64	42.01	41.65	42.02
c/a	1.05	1.08	1.05	1.98
n = 2				
	3.87	4.10	4.90	5.31
P_x	2.43	2.67	2.42	2.60
P_y	7.23	7.64	7.20	7.69
P_z	44.37	45.02	44.36	45.00
c/a	1.06	1.09	1.06	1.09

Fig. 3.17 and 3.18 represents that total DOS for $(HfO_2)_1/(ZrO_2)_1$ and $(HfO_2)_2/(ZrO_2)_2$ thus, a structure with 50% of HfO_2 layers and 50% ZrO_2 layers as shown in Fig. 3.17. such that there is one layer of Hf-O and next is of Zr-O. The band gap predicted for such a case is 4.09 eV and 4.26 eV for PBE and PBE+U, respectively.

To further improve the band gap, mBJ is utilized with primitive structures, and it can be seen that the bandgap has improved to a value of 5.06 eV and 5.77 eV for mBJ and mBJ+U respectively. Meanwhile, to introduce the broader layer of almost 0.2nm thick, the two layers of Hf and Zr are introduced in the super-cell. Thus, for $(HfO_2)_2/(ZrO_2)_2$ the band gap calculated is 3.87 eV and 4.10 eV for PBE and PBE+U, respectively. For mBJ and mBJ+U are 4.90 eV and 5.31 eV, respectively.

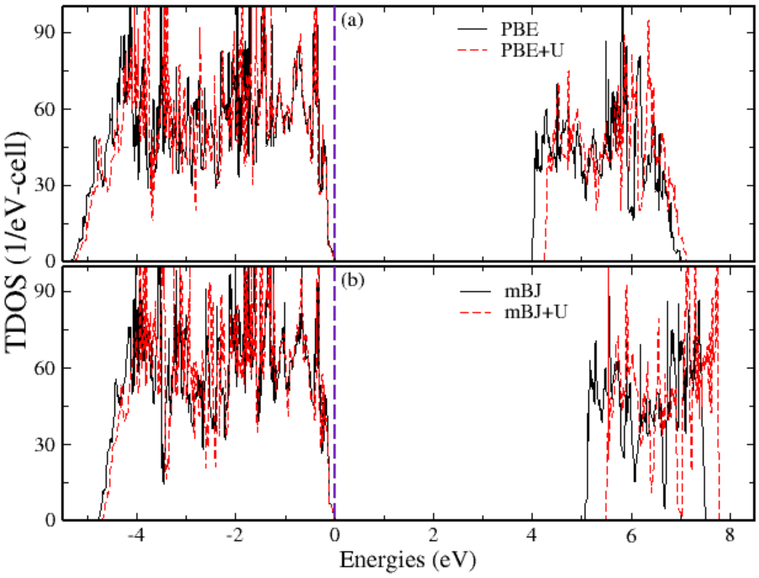

Figure 3.17: Total DOS of $(HfO_2)_1/(ZrO_2)_1$ for orthorhombic phase (a) PBE and PBE+U (b) mBJ and mBJ+U. The zero of energy corresponds to the top of valence bands E_{VBM}.

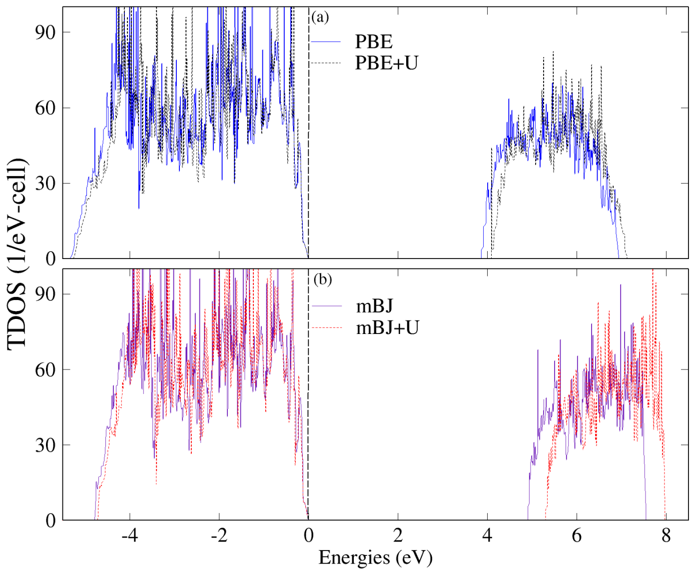

Figure 3.18: Total DOS of $(HfO_2)_2/(ZrO_2)_2$ for orthorhombic phase (a) PBE and PBE+U (b) mBJ and mBJ+U. The vertical dotted line represents the E_{VBM} set at zero.

Tetragonal

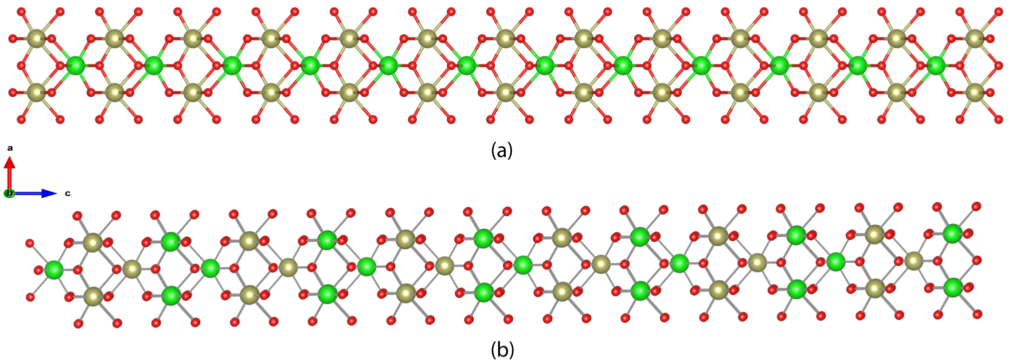

Figure 3.19: Structural representation of (a) $(HfO_2)_1/(ZrO_2)_1$, (b) $(HfO_2)_2/(ZrO_2)_2$ in tetragonal phase.

The optimized crystal structure of $(HfO_2)_n/(ZrO_2)_n$ with n = 1 and 2 are represented in Fig. 3.19. The band gaps for $(HfO_2)_1/(ZrO_2)_1$ and $HfO_2)_2/(ZrO_2)_2$ along with spontaneous polarization in is described in Table. 3.13

Table 3.13: Computed band gap energies (E_g) in eV and spontaneous polarization P_x, P_y and P_z in μCcm^{-2} for $(HfO_2)_n/(ZrO_2)_n$, n = 1, 2 in tetragonal phase.

	PBE	PBE+U	mBJ	mBJ+U
n = 1				
	4.24	4.43	5.27	5.77
P_x	0.04	3.94	3.34	3.91
P_y	0.42	8.01	7.20	8.03
P_z	3.32	4.01	3.29	4.00
c/a	1.45	1.46	1.45	1.46
n = 2				
	4.18	4.46	5.16	5.85
P_x	0.00	2.67	2.42	2.60
P_y	0.26	7.64	7.20	7.69
P_z	4.26	5.02	4.30	5.00
c/a	1.45	1.46	1.45	1.46

The tetragonal phase lacks distinguishable polarization. However, while calculating using eqs. 3.5 polarization is observed, which are $P_z = 3.32$ μCcm^{-2} and $P_z = 4.26$ μCcm^{-2} for $(HfO_2)_1/(ZrO_2)_1$ and $(HfO_2)_2/(ZrO_2)_2$, respectively along z-axis. The other directions also found to have small value for spontaneous polarization that is almost $P_x = 0.04$ μCcm^{-2} and $P_y = 0.42$ μCcm^{-2}.

TDOS for $(HfO_2)_1/(ZrO_2)_1$ and $(HfO_2)_2/(ZrO_2)_2$ are illustrated in Fig. 3.20 and 3.21 the band gap is 4.24 eV and 4.43 for $(HfO_2)_1/(ZrO_2)_1$ for PBE and

PBE+U, respectively. The band gap is modified using mBJ have value of 5.27 eV and 5.77 eV for mBJ and mBJ+U, respectively. For $(HfO_2)_2/(ZrO_2)_2$ the estimated band gaps are 4.18 eV and 4.46 eV for PBE and PBE+U, respectively. While for mBJ and mBJ+U, 5.16 eV and 5.85 eV, respectively.

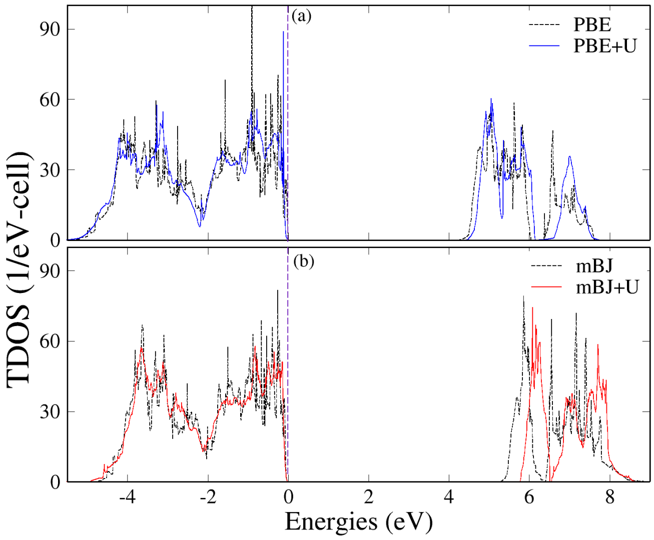

Figure 3.20: Total DOS for tetragonal phase $(HfO_2)_1/(ZrO_2)_1$ (a) PBE, PBE+U (b) mBJ, mBJ+U.

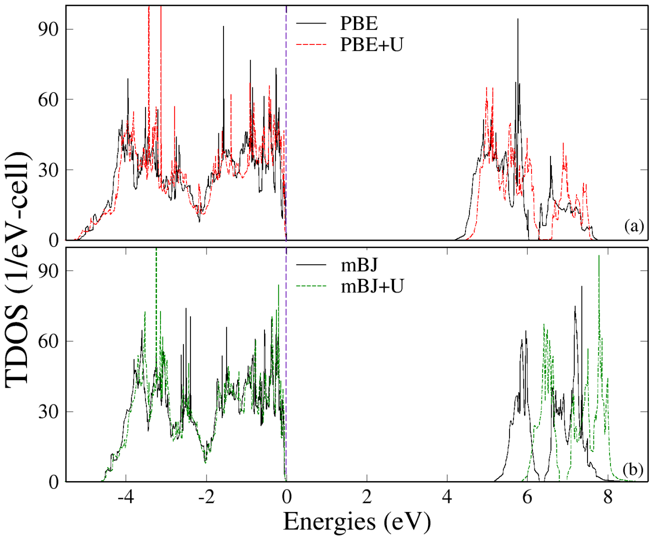

Figure 3.21: Total DOS for tetragonal phase $(HfO_2)_2/(ZrO_2)_2$ (a) PBE, PBE+U (b) mBJ, mBJ+U.

Overall, it has been observed that the band gaps for primitive structures of ZrO_2 are smaller as compared to those of HfO_2 as it has been described above that Zr has more d-states just below the E_{VBM} as compared to Hf. As the Zr-concentration increases, the more and more d-states starts to accumulate on E_{VBM} ($E_{VBM} = 0$) but still the results are underestimated as compared to the experimental. However, the reduction in the band gap for the layered configurations could be explained because of the incorporation of 4d orbitals of Zr, which downshift the CBM.

Although the insertion of $U_d = 3$ eV has improved the band gap for both phases, the trend remains the same. The incorporation of Zr modifies the conduction band structure of HfO_2. The results of the total density of state show good coherence with the literature; as reported earlier [90], the addition of Zr into HfO_2 causes a few energy states to move up into the band gap, and impurity energy lies closer to the bottom of the conduction band. Consequently, electron transition level spacing is expected to decrease, and hence the conductivity of the whole system is increased [90]. Nevertheless, it is evident from the observed results that alloying of HfO_2 with other materials can cause significant changes in energy gap (E_g) and ferroelectricity of HfO_2. For $(HfO_2)_1/(ZrO_2)_1$ the band gaps and spontaneous polarization is found be smaller as comapared to $(HfO_2)_2/(ZrO_2)_2$ for both orthrhombic and tetragonal phase. It has been analyzed that for $(HfO_2)_2/(ZrO_2)_2$ the c/a ratio is increased the and thus due to increased structural distortions the value of spontaneous polarization is increased.

Part IV

Conclusion

Using first-principle computations on tetragonal, monoclinic, orthorhombic phases of ZrO_2 and HfO_2 to investigate the structural, electronic, optical, and ferroelectric properties using the PBE and mBJ potentials. As well as the Born effective charges and dielectric properties are also investigated. The following conclusions have been obtained. First, lattice parameters obtained after structural optimization agree with the previously reported results. Second, for all phases of ZrO_2 and HfO_2 under discussion, the electronic contributions ϵ_{ij}^{∞} to the static dielectric constant of value (range from 5 to 6.5) and neither strongly anisotropic nor strongly dependent on the structural phase, while the ionic contributions ion ϵ_{ij}^{ion} are much larger, more anisotropic, and more sensitive to the structural phases. Third, the average dielectric constant for three phases of ZrO_2 and HfO_2 decreases in the sequence of tetragonal, orthorhombic, and monoclinic phases.

The magnitudes of the Born effective charges of the Zr/Hf and oxygen atoms are more significant than their nominal ionic valences (+4 for Zr/Hf and -2 for O), indicating a solid dynamic charge transfer from Zr/Hf atoms to O atoms and a mixed covalent-ionic bonding in all three phases of both twin oxides. In the electronic properties, the computed spectra for the density of states are discussed. To calculate electronic properties, a complete comparison of three phases of ZrO_2 and HfO_2 along with alloying of hafnia with Zr-atoms has been reported using PBE, PBE+U, mBJ, and mBJ+U methods in combination. Further, the on-site Coulomb interactions have been included for the 5d/4d orbital of the Hf/Zr atom for all phases to solve the discrepancies between experimental and predicted excited states properties, improving the description of the electronic properties. The optimal value of $U^d = 3$ eV is used. The optimal values for band gaps are obtained using PBE+U and mBJ potentials. In addition to optical and electronic properties, ferroelectric properties have also been investigated. For primitive bulk structures, the tetragonal and monoclinic found have non-polar structures, thus contributing significantly less or no spontaneous polarization. In contrast, the ortho-phase for both oxides, even in super-cell of hafnia with Zr-content, has shown a significant amount of spontaneous polarization.

Part V

Future Work

The calculations here presented mainly consist of a study of the electronic and ferroelectric properties of primitive structures. However, the mechanisms proposed here could be tested within large-scale systems such as heterostructures accompanied by a study of layered structures with the incorporation of other d-orbital atoms dopants on the cation site. The tetragonal phase is reported to have higher dielectric constants but low ferroelectricity. Furthermore, studies have shown that tetravalent doping usually favors the tetragonal phase over the orthorhombic phases of HfO_2 and ZrO_2. It can lead to a change in polarization, most probably polarization switching.

Infrastructure acknowledgement

The computations/simulations for DFT analysis of HfO_2 and ZrO_2 were performed on resources provided by Sigma2 - the National Infrastructure for High Performance Computing and Data Storage in Norway

Bibliography

[1] J. Robertson, "High dielectric constant oxides," EPJ Appl. Phys. **28**, 265–291 (2004).

[2] C. Fiegna, H. Iwai, T. Wada, M. Saito, E. Sangiorgi, and B. Riccò, "Scaling the mos transistor below 0.1 /spl mu/m: methodology, device structures and technology requirements," IEEE Transactions on Electron Devices **41**, 941–951 (1994).

[3] G. D. W. *et al.*, "High-k gate dielectrics: current status and materials properties considerations," Journal of Applied Physics **89**, 5243–5275 (2001).

[4] K. van Benthem, C. Elsässer, and R. H. French, "Bulk electronic structure of srtio3: experiment and theory," Journal of Applied Physics **90**, 6156–6164 (2001).

[5] K. J. Hubbard and D. G. Schlom, "Thermodynamic stability of binary oxides in contact with silicon," Journal of Materials Research **11**, 2757–2776 (1996).

[6] O. B. *et al.*, "Spectroellipsometric assessment of hfo2 thin films," Thin Solid Films **517**, 453–455 (2006).

[7] y. K. M.N.Jones and D. P. Norton, "Dielectric constant and current transport for hfo_2 thin films on ito," Applied Physics A: Materials Science & Processing **81**, 285–288 (2005).

[8] D. A. Buck, "Ferroelectrics for digital information storage and switching," Phd thesis, Massachusetts Institute of Technology (1952).

[9] R. Lous, "Ferroelectric memory devices," Appl. Phys. **85**, 4118 (2011).

[10] G. H. Haertling, "Ferroelectric ceramics: history and technology," Journal American Ceramic Society **797-818**, 6156–6164 (1999).

[11] N. S. *et al.*, "Ferroelectric thin films: review of materials, properties and applications," Journal of Applied Physics **100**, 109901 (2006).

[12] W. Yang and T. Zhu, "Switch-toughening of ferroelectrics subjected to electric fields," Journal of the Mechanics and Physics of Solids **46**, 291–311 (1998).

[13] J. F. I. *et al.*, "Scaling effects in perovskite ferroelectrics: fundamental limits and process-structure-property relations," Journal American Ceramic Society **99**, 2537–2557 (2016).

[14] R. R. (Ed.), *Thin film ferroelectric materials and devices*, Vol. 3 (Springer Science & Business Media, 2013), pp. VII, 249.

[15] T. S. B. *et al.*, "Ferroelectricity in hafnium oxide thin films," Appl. Phys. Lett. **99**, 102903–8 (2011).

[16] U. S. *et al.*, "Impact of different dopants on the switching properties of ferroelectric hafniumoxide," Jpn. J. Appl. Phys. **53**, 08LE02–5 (2014).

[17] M. H. P. *et al.*, "Ferroelectricity and antiferroelectricity of doped thin hfo2-based films," Adv. Mater. **27(11)**, 1811–31 (2015).

[18] K. K. K. Kita and A. Toriumi, "Permittivity increase of yttrium-doped HfO_2 through structural phase transformation," Appl. Phys (2005).

[19] Y. M. J.H. Choi and J. Chang, "Development of hafnium based high-k materials," A Review. Mater. Sci. Eng. R Reports **86**, 102906 (2011).

[20] J. Müller, P. Polakowski, S. Mueller, and T. Mikolajick, "Ferroelectric hafnium oxide based materials and devices: assessment of current status and future prospects," ECS Journal of Solid State Science and Technology **4** (2015).

[21] S. M. M . A. Alam and Y. D. Peide, "A critical review of recent progress on negative capacitance field-effect transistors," Appl. Phys. Lett. **114**, 090401 (2019).

[22] M. H. P. *et al.*, "Study on the size effect in hf0.5zr0.5o2 films thinner than 8-nm before and after wake-up field cycling," Phys. Status Solidi RRL **107**, 192907 (2014).

[23] M. Y. *et al.*, "Impact of specific failure mechanisms on endurance improvement for hfo2-based ferroelectric tunnel junction memory," 2018 IEEE International Reliability Physics Symposium (IRPS), 6D.2-1-6D.2–6 (2018).

[24] R. M. J. T. Mazumder and S. Tripathy, "Theoretical investigation on structural, electronic, optical and elastic properties of tio2, sno2, zro2 and hfo2 using scan meta-gga functional: a dft study," Materials Chemistry and Physics **254**, 123474 (2020).

[25] J. L. *et al.*, "Electronic structures and optical properties of monoclinic zro2 studied by first-principles local density approximation + u approach.," J Adv Ceram **6**, 43–49 (2017).

[26] H. A. R. Terki G. Bertrand and C. Coddet, "Structural and electronic properties of zirconia phases: a fp-lapw investigations," Materials Science in Semiconductor Processing **9**, 1006–1013 (2006).

[27] D. A. Neumayer and E. Cartier, "Materials characterization of zro_2–sio_2 and hfo_2–sio_2 binary oxides deposited by chemical solution deposition," Journal of Applied Physics **90**, 1801 (2001).

[28] H. S. *et al.*, “Zirconia and hafnia polymorphs – ground state structural properties from diffusion monte carlo,” Phys. Rev. Materials **2**, 075001 (2018).

[29] R. A. B. J. E. Jaffe and M. Gutowski, “M. low-temperature polymorphs of zrO_2 and hfO_2: a density-functional theory study,” Phys. Rev. B **72**, 144107 (2005).

[30] X. Zhao and D. Vanderbilt, “Phonons and lattice dielectric properties of zirconia,” Phys. Rev. B **65**, 075105 (2002).

[31] X. Z. *et al.*, “First-principles study of structural, vibrational and lattice dielectric properties of hafnium oxide,” Phys. Rev. B **65**, 233106 (2002).

[32] U. von Barth, “Basic density-functional theory,” Physica Scripta. **T109**, 9 (2004).

[33] David Sholl and Janice A Steckel, *Density functional theory - a practical introduction*, Vol. 49, 3 (John Wiley & Sons Inc., 2009), pp. 485–485.

[34] J. C. Slater, *Quantum theory of atomic structure*, tech. rep. (1960).

[35] M. Born, “Physical aspects of quantum mechanics,” Nature **119**, 354–357.

[36] P. Hohenberg and W. Kohn, “Inhomogeneous electron gas.,” Phys. Rev. **136**, B864–B871 (1964).

[37] W.Kohn and L. J. Sham, “A simple effective potential for exchange,” Phys. Rev. **140**, A1133–A1138 (1965).

[38] W.Kohn and P. Vashishta, *General density functional theory* (Springer Boston MA., 1983), pp. 79–147.

[39] P. Ziesche, S. Kurth, and J. P. Perdew, “Density functionals from lda to gga,” Computational Materials Science **11**, 122–127 (1998).

[40] D. C. Langreth and M. J. Mehl, “Beyond the local-density approximation in calculations of ground-state electronic properties .,” Phys. Rev. B **28**, 1809–1834 (1982).

[41] F. J. J. Wiley and Chichester, *Introduction to computational chemistry* (John Wiley & Sons., 2007), pp. 79–664.

[42] R. G. Parr and W. Yang, *Density functional theory of atoms and molecules* (Oxford University Press Oxford., 1989).

[43] J. S. Blakemore, *Solid state physics* (Cambrige University Press, 1985), pp. 30–500.

[44] J. Kohanoff and N. Gidopulos, *Handbook of molecular physics and quantum chemistry*, Vol. 3 (Rutherford Appleton Laboratory Oxfordshire, 2003).

[45] R. O. Jones and O. Gunnarsson, "The density functional formalism, its applications and prospects.," Rev. Mod. Phys. **61**, 689–746 (1989).

[46] L. T. P. Haas and P. Blaha, "Calculation of the lattice constant of solids with semi local functionals.," Phys. Rev. B **79**, 085104 (2009).

[47] J. P. Perdew and Y. Wang, "Accurate and simple analytic representation of the electron-gas correlation energy," **45**, 13244–13249 (2018).

[48] K. B. J. P. Perdew and M. Ernzerhof, "Generalized gradient approximation made simple," Phys. Rev. Lett. **77**, 3865–3868 (1997).

[49] J. P. P. *et al.*, "Restoring the density-gradient expansion for exchange in solids and surfaces," Phys. Rev. Lett. **100**, 136406 (2008).

[50] S. L. D. *et al.*, "Electron-energy-loss spectra and the structural stability of nickel oxide: an lsda+u study.," Phys. Rev. B **57**, 1505–1509 (1998).

[51] M. Cococcioni and S. de Gironcoli, ". linear response approach to the calculation of the effective interaction parameters in the lda + u method," Phys. Rev. B **71**, 16 (2005).

[52] D. Sholl and J. Steckel, *Density functional theory: a practical introduction* (John Wiley & Sons, 2009), pp. 20–270.

[53] G. Kresse and J. Hafner, “Ab initio molecular dynamics for open-shell transition metals,” Phys. Rev. B **48**, 13115–13118 (1993).

[54] G. Kresse and J.Furthmüllerb, “Efficiency of ab-initio total energy calculations for metals and semiconductors using a plane-wave basis set,” Computational Materials Science **6**, 15–50 (1996).

[55] G. Kresse and J. Furthmüller, “Efficient iterative schemes for ab initio total-energy calculations using a plane-wave basis set,” Phys. Rev. B **54**, 11169–11186 (1996).

[56] K. B. J. P. Perdew and M. Ernzerhof, “Generalized gradient approximation made simple,” Phys. Rev. Lett. **77**, 3865–3868 (1997).

[57] H. J. Monkhorst and J. D. Pack, “Special points for brillouin-zone integrations,” Phys. Rev. B **13**, 5188–5192 (1976).

[58] Y. Z. *et al.*, “A comparison study of the born effective charges and dielectric properties of the cubic, tetragonal, monoclinic, ortho-i, ortho-ii and ortho-iii phases of zirconia,” Solid State Sciences **81**, 58–65 (2018).

[59] L. J. *et a.l*, “Optical properties of monoclinic hfO_2 studied by first-principles local density approximation+ u approach,” Appl. Phys. Lett. **103**, 071916 (2013).

[60] Z. L. T. Tan and Y. Li, “First-principles calculations of electronic and optical properties of ti-doped monoclinic hfo$_2$,” Journal of Alloys and Compounds **510**, 78–82 (2012).

[61] J. Adam and M. Rogers, “, the crystal structure of zrO_2 and hfO_2,” Acta Crystallogr. **64**, 10 (1959).

[62] M. H. *et al.*, “Stabilizing the ferroelectric phase in doped hafnium oxide.,” . J. Appl. Phys. **118**, 072006 (2015).

[63] A. K. R. Materlik C. Künne an, “The origin of ferroelectricity in $Hf_{1-x}Zr_xO_2$: a computational investigation and a surface energy model,” J. Appl. Phys. **117**, 134109 (2015).

[64] I. M. *et al.*, “Texture, twinning and metastable “tetragonal” phase in ultrathin films of hfO_2 on a si substrate,” J. Electrochem . Soc. **67**, 1441 (2009).

[65] W. Z. *et al.*, “Electronic structure differences in zr$O-2$ vs hf$O-2$ zr$O-2$,” J. Phys. Chem. A **109(50)**, 11521–11525 (2005).

[66] G. Teufer, “The crystal structure of tetragonal zr$O-2$,” Acta Cryst. **15**, 1187 (1962).

[67] G. M. R. *et al.*, “First-principles study of dynamical and dielectric properties of tetragonal zirconia,” Phys. Rev. B **64**, 134301:1–7 (2001).

[68] J. L. *et al.*, “Optical properties of monoclinic hfo2 studied by first-principles local density approximation + u approach,” Applied Physics Letters **103**, 071916 (2013).

[69] X. Y. Zhao and D. Vanderbilt, “Phonons and lattice dielectric properties of zirconia,” Phys. Rev. B **65**, 075105 (2002).

[70] G. M. R. *et al.*, “First-principles investigation of high-k dielectrics: comparison between the silicates and oxides of hafnium and zirconium,” Phys. Rev. B **69**, 184301:1–10 (2004).

[71] M. T. L. *et al.*, “The dielectric properties of yttria-stabilized zirconia,” Mater. Lett. 7 **7**, 437–440 (1989).

[72] A. Dwivedi and A. N. Cormack, “A computer simulation study of the defect structure of calcia-stabilized zirconia,” **61**, 1–22 (1990).

[73] I. P. *et al.*, “High-throughput screening of inorganic compounds for the discovery of novel dielectric and optical materials,” Sci Data 4 **4(1)**, 160134 (2017).

[74] S. N. *et al.*, "Chemical bonding and born charge in 1t-hfs$_2$r," npj 2D Materials and Applications, 5, 45 **5**, 45 (2021).

[75] T. Shimizu, "Ferroelectricity in hfO_2 and related ferroelectrics," Journal of the Ceramic Society of Japan **126**, 667–674 (2018).

[76] R. E. Cohen, "Origin of ferroelectricity in perovskite oxides," Journal of the Ceramic Society of Japan **126**, 601–614 (2018).

[77] J. L. *et al.*, "Electronic structures and optical properties of monoclinic zro2 studied by first-principles local density approximation + u approach," J. Adv. Cer. **6**, 43–49 (2017).

[78] P. C. *et al.*, "X-ray photoemission spectroscopy and optical reflectivity of yttrium-stabilized zirconia," Phys. Rev. B **50**, 4292–4296 (1994).

[79] V. A. R. I. A. Shanshoury and I. A. Ibrahim, "Polymorphic behavior of thin evaporated films of zirconium and hafnium oxides," J. Am. Ceram. Soc **53**, 264–268 (1970).

[80] R. Zhang*et al.*, "First-principles study of direct band gap semiconductors xs$_2$ (x = zr and hf) with orthorhombic symmetry," J. Phys. D: Appl. Phys. **55** (2022).

[81] H. J. *et al.*, "Electronic band structure of zirconia and hafnia polymorphs from the gw perspective," Phys. Rev. B **81**, 085119 (2010).

[82] S. S. *et al.*, "Band alignment issues related to hfo$_2$/sio$_2$/p-si gate stacks," J. Appl. Phys. **100**, 122907 (2004).

[83] R. H. F. *et al.*, "Experimental and theoretical determination of the electronic structure and optical properties of three phases of zro$_2$," Phys. Rev. B **49**, 5133–5142 (1974).

[84] A. Foster*et al.*, "Structure and electrical levels of point defects in monoclinic zirconia," Phys. Rev. B **64**, 224108 (2001).

[85] A. D. Beckea and E. R. Johnson, "Self-consistent equations including exchange and correlation effects," J. Chem. Phys. **126**, 174104 (2006).

[86] P. O. *et al.*, "Accurate prediction of band gaps and optical properties of hfo$_2$," J. Phys. D: Appl. Phys. **49**, 395301 (2016).

[87] S. S. T. Mikolajick and U. Schröder, "Ferroelectric hafnium oxide for ferroelectric random-access memories and ferroelectric field-effect transistors," MRS Bulletin. **43**, 340–346 (2018).

[88] E. Tsymbal and H. Kohlstedt, "Tunneling across a ferroelectric," Science **313**, 181–183 (2006).

[89] B. Max, T. Mikolajick, M. Hoffmann, S. Slesazeck, and T. Mikolajick, "Retention characteristics of hf0.5zr0.5o2-based ferroelectric tunnel junctions," 2019 IEEE 11th International Memory Workshop (IMW), 1–4 (2019).

[90] Z. Y. *et al.*, "Metal dopants in hfo$_2$-based rram: first principle study," J. Semicond. **35**, 042002 (2014).